

Non-Axisymmetric Precession of Magnetars and Fast Radio Bursts

I. WASSERMAN,^{1,2} J. M. CORDES,¹ S. CHATTERJEE,¹ AND G. BATRA¹

¹*Cornell Center for Astrophysics and Planetary Science, Cornell University*

²*Laboratory for Elementary Particle Physics, Cornell University*

ABSTRACT

The repeating FRBs 180916.J0158 and 121102 are visible during periodically-occurring windows in time. We consider the constraints on internal magnetic fields and geometry if the cyclical behavior observed for FRB 180916.J0158 and FRB 121102 is due to precession of magnetars. In order to frustrate vortex line pinning we argue that internal magnetic fields must be stronger than about 10^{16} Gauss, which is large enough to prevent superconductivity in the core and destroy the crustal lattice structure. We conjecture that the magnetic field inside precessing magnetars has three components, (1) a dipole component with characteristic strength $\sim 10^{14}$ Gauss; (2) a toroidal component with characteristic strength $\sim 10^{15} - 10^{16}$ Gauss which only occupies a modest fraction of the stellar volume; and (3) a disordered field with characteristic strength $\sim 10^{16}$ Gauss. The disordered field is primarily responsible for permitting precession, which stops once this field component decays away, which we conjecture happens after ~ 1000 years. Conceivably, as the disordered component damps bursting activity diminishes and eventually ceases. We model the quadrupolar magnetic distortion of the star, which is due to its ordered components primarily, as triaxial and very likely prolate. We address the question of whether or not the spin frequency ought to be detectable for precessing, bursting magnetars by constructing a specific model in which bursts happen randomly in time with random directions distributed in or between cones relative to a single symmetry axis. Within the context of these specific models, we find that there are precession geometries for which detecting the spin frequency is very unlikely.

Keywords: stars: neutron — stars: magnetars — Fast Radio Bursts: FRB 121102 — Fast Radio Bursts: FRB 180916

1. INTRODUCTION

The relatively long 16.4 day period of FRB 180916.J0158 (Chime/Frb Collaboration et al. 2020) and the even longer 160 day period of FRB 121102 (e.g. Cruces et al. 2021) suggest precession of magnetars deformed by strong internal magnetic fields (Levin et al. 2020; Zanazzi & Lai 2020). However, to date no evidence for a spin period has been reported for either of these FRBs (e.g. Zhang et al. 2018; Li et al. 2021). One possibility is that not enough bursts have been detected yet for either FRB to reveal their spin frequencies, presuming that the underlying engine is a magnetar. But a second possibility is that the physical nature of the repeating bursts might prevent detecting a spin frequency even in upcoming surveys that detect far larger numbers of individual outbursts.

The important phenomenological questions motivating this paper are:

1. Should the spin period be detectable in FRBs that reappear periodically because of precession ?
2. Is it possible for there to be no evidence for either a spin period or a precession period for FRBs associated with a precessing magnetar ?

Recently, evidence for a short ≈ 0.2 second period has been presented by [The CHIME/FRB Collaboration et al. \(2021\)](#) from analysis of the light curve of a *single* outburst lasting ≈ 4 seconds. This report lends urgency to addressing these two questions, and raises other issues we shall not address here, such as whether or not the 0.2 second period is due to magnetar spin, and, if it is, what the implications are for spindown, internal magnetic fields and precession.

In order to address these two questions, we first examine what the detection of precession tells us about the internal magnetic fields of the magnetars presumed to be the sources of the FRBs. [Shaham \(1977\)](#) showed that the pinning of (crustal) superfluid neutron vortex lines can prevent slow precession, and [Link \(2003\)](#) showed that pinning of neutron vortices to flux tubes associated with proton superconductor is likely wherever superfluid and superconductor coexist in the core of a neutron star. Moreover, for a neutron star rotating with period P and precessing with period P_p the moment of inertia of the region where neutron vortices are pinned must be $\lesssim P/P_p \approx 10^{-7} P(\text{s})/(P_p/100\text{d})$ times the total moment of inertia of the star for slow precession to be possible. We can't rule out that FRB 121102 and FRB 180916.J0158 are both fine-tuned to the accuracy necessary to permit slow precession. However, we regard it as far likelier that the magnetic fields in the interiors of these magnetars are large enough to destroy proton superconductivity (and perhaps even neutron superfluidity).

§2.1 is devoted to discussing constraints on the internal magnetic fields that would be consistent with precession. We propose a specific model for the magnetic field that has three distinct components: in order of typical magnetic field strength these are a dipole field, a toroidal field, both of which are ordered, and a disordered field. We develop this model in §2.2, where we are led inevitably to the conclusion that the quadrupole distortion of the star is triaxial, and most likely somewhat prolate. We also propose that a magnetar may only precess for a relatively short portion of its life lasting perhaps 1000 years.

§2.3 develops results on triaxial precession necessary for the more phenomenological modelling done in §3. In particular, we show that rather large amplitude precession can be excited with relatively little fractional expenditure of magnetic energy, a natural consequence of the fact that magnetic energy is substantially larger than rotational energy in magnetars. We also consider two distinct types of effects due to spindown. In §2.4 we develop the timing model relating observer time to precession phase when spindown is included. There are two effects, the familiar long term spindown but also a cyclical effect specific to precessing pulsars that has period P_p ([Cordes 1993](#)). In §2.5 we investigate the secular effect of spindown on the precession amplitude and phase, generalizing work done by [Goldreich \(1970\)](#) for oblate axisymmetric precession to triaxial precession. We outline a simple phase diagram for this more complicated problem that is more complex than what arises for oblate, axisymmetric precession.

Finally, in §3 we develop a very specific model in which we assume that FRBs are tied to magnetar outbursts that occur randomly in time and point in random directions about some reference axis, which we take to be (but need not be) the magnetic dipole axis. We show that it is impossible to detect either the spin frequency or the precession period if the outbursts can point in any direction, which is not a big surprise. However, we also find that the spin frequency ought to be easy to detect in some cases and much harder in others, depending on specific characteristics of the precession model and the distribution of beam directions of the outbursts.

From a qualitative point of view, we offer two simple reasons that the outbursts underlying FRBs may occur randomly in time. Although tautological, one explanation is that the physical mechanism triggering the bursts simply is stochastic temporally, with burst directions that are random within some boundaries. Another is that the times between burst triggers are irregular but correlated, perhaps because there is a characteristic time for the burst phenomenon to reload, but associated with each outburst is a random time offset, possibly as large as the spin period, related to where the burst is triggered within the magnetar magnetosphere. The bursts may point in a large range of directions because they involve plasma moving relativistically along open magnetic field lines, leading to highly focussed energy output in directions ranging from close to the magnetic dipole axis to perpendicular to the light cylinder. Alternatively, bursts may originate from a set of distinct, concentrated regions in the magnetosphere of a magnetar that turn on and off stochastically, with each region beaming energy outward in a different direction.

In a companion paper we address the challenge of uncovering an underlying FRB spin frequency in a more general, phenomenological way that does not rely on as specific a model for bursts from rotating magnetars as we develop in §3. The model presented in this paper can be regarded as a definite physical set up that realizes the general conditions for hiding the spin frequency of an FRB-inducing magnetar developed in the companion paper.

2. INTERNAL MAGNETIC FIELDS AND TRIAXIAL PRECESSION

2.1. Internal Magnetic Fields that Permit Slow Precession

Previous work has focussed primarily on precession arising from oblate axisymmetric distortion due to magnetic stresses (e.g. Levin et al. 2020; Zanazzi & Lai 2020). Here, we examine what internal magnetic structure may be required for precession to occur, and highlight distinctive features that arise when the distortion is not axisymmetric and possibly prolate.

The internal magnetic structure of magnetars is not well-studied. In general, magnetohydrodynamic (MHD) studies of the magnetic fields in normal conductors have shown that there are *no* stable magnetic field configurations in barotropic normal fluids (Lander & Jones 2012; Mitchell et al. 2015), but that stable, axisymmetric configurations may exist in stably stratified fluids (Reisenegger 2009; Akgün et al. 2013; Mitchell et al. 2015). Braithwaite (2009) and Akgün et al. (2013) argued that there may be stable magnetic field configurations in stably stratified stars whose poloidal fields are *much weaker* than their toroidal fields. Glampedakis & Lasky (2016) argued that the *equilibrium* magnetic fields in non-barotropic normal fluid stars can be specified freely if they are axisymmetric, but not if they are non-axisymmetric. At the strong fields we envision, magnetization due to Landau quantization of core electrons also affects stability (Rau & Wasserman 2021; Suh & Mathews 2010). Relativistic equilibria have been computed using realistic equations of state (e.g. Cardall et al. 2001; Kiuchi & Yoshida 2008; Friebe & Rezzolla 2012); equilibria were only found to exist if the maximum internal magnetic field strength is $\lesssim 10^{18}$ G, which is a significant indication of limitations imposed by overall dynamical stability, but does not assess MHD stability. Of course, stability constraints are not necessarily relevant if the magnetic field is time-dependent, although presumably field configurations that are MHD unstable vary rather rapidly on timescales set by the local Alfvén speed and the lengthscale of variation.

Overall, these studies suggest that the internal magnetic fields of magnetars could be considerably stronger than their dipole (surface) magnetic field.

Another, rather different, argument also suggests strong internal magnetic fields. Once the core of the star cools below $\approx 10^9$ K core protons become superconducting unless the internal magnetic field is stronger than the second critical field strength

$$H_{c2} = \frac{\Phi_0}{2\pi\xi_p^2} = \frac{(\pi m_p^* \Delta_p / p_{F,p})^2 c}{2e\hbar} \approx \frac{9 \times 10^{15} (\Delta_p / m_e)^2 (m_p^* / 0.7m_p)^2}{(p_{F,p} / 100\text{MeV})^2} \text{ Gauss} \quad (1)$$

where Δ_p is the proton gap, $p_{F,p}$ is the proton Fermi momentum, m_p^* is the proton effective mass, $\xi_p = \hbar p_{F,p} / \pi m_p^* \Delta_p$ is the coherence length and $\Phi_0 = \pi \hbar c / e$ is the flux quantum. Proton gap calculations are complicated by many body effects at high densities (Zuo et al. 2008; Gezerlis et al. 2014; Dong et al. 2017; Guo et al. 2019) but indicate that $\Delta_p \simeq 0.5 \text{ MeV} \approx m_e$ near nuclear density $n_{\text{nuc}} = 0.16 \text{ fm}^{-3}$, where $p_{F,p} \approx 100 \text{ MeV}$; Δ_p decreases to zero at densities $\gtrsim 2n_{\text{nuc}}$. Of course, it is also possible that protons are superconducting but magnetic field strengths at the inner boundary of the (normal) crust are below the first critical field strength

$$H_{c1} \approx \frac{2 \times 10^{14} (p_{F,p} / 100 \text{ MeV})^3 \ln \kappa}{(m_p^* / 0.7m_p)} \text{ Gauss}, \quad \kappa \approx \frac{4.8 (m_p^* / 0.7m_p)^{3/2} (\Delta_p / m_e)}{(p_{F,p} / 100 \text{ MeV})^{5/2}},$$

in which case magnetic fields would not penetrate into the superconductor in equilibrium if entering from the outside. However, very likely magnetic flux in the core is “left over” from before it cooled enough to become superconducting (e.g. Baym et al. 1969), in which case the proton superconductor in the core is in a “mixed state” with $H_{c2} > H > H_{c1}$. Quadrupolar deformations due to magnetic fields are

$$\epsilon_{\text{mag}} = \frac{\beta_2 H B R^4}{GM^2} \approx \frac{2 \times 10^{-6} \beta_2 B_{15}^2 R_{10}^4}{M_{1.4}^2} \times \frac{H}{B} \quad (2)$$

for magnetic induction $B = 10^{15} B_{15}$ Gauss, stellar radius $R = 10 R_{10}$ km and mass $M = 1.4 M_{1.4} M_\odot$, where $H/B = 1$ for a normal conductor but $H/B > 1$ for a type ii superconductor (e.g. Jones 1975; Cutler 2002; Wasserman 2003; Henriksson & Wasserman 2013; Akgün & Wasserman 2008). The parameter β_2 depends on the structure of the neutron star and of its internal magnetic field, and represents how effectively the magnetic forces cause quadrupolar deformation.

The superconductor is type ii as long as $\kappa > 1/\sqrt{2}$, which is the case throughout much of the region where protons are superconducting. In a type ii superconductor, magnetic flux is organized into an array of thin flux tubes that have

an areal density $eB/\pi\hbar c \approx 5 \times 10^{21} B_{15} \text{ cm}^{-2}$. If the neutrons are also superfluid their vorticity would be confined into thin vortex lines with a much lower areal density $\mu_n \Omega/\pi\hbar \approx 3 \times 10^4 (\mu_n/m_n)/P(\text{s}) \text{ cm}^{-2}$ for a rotation period $P(\text{s})$ seconds, where μ_n/m_n is the neutron chemical potential in units of the neutron rest mass. Unless the relative velocity between flux lines and vortex lines is big enough, which may be true if the precession amplitude remains sufficiently large (Link & Cutler 2002), vortex lines will pin to flux lines (Link 2003), which frustrates slow precession (Shaham 1977). This problem can be avoided entirely if the core of the neutron star is hot enough that neutrons remain normal: neutron gaps are $\sim 10 - 100 \text{ keV} \simeq 10^{8-9} \text{ K}$ (Zuo et al. 2008; Gezerlis et al. 2014; Dong et al. 2017; Guo et al. 2019). Calculations by Potekhin & Chabrier (2018) indicate that the core of a magnetar may cool below a few $\times 10^8 \text{ K}$ within $\lesssim 100$ years of forming, so neutrons may be normal in some but not all of the core of a $\lesssim 100$ year old magnetar unless the maximum neutron critical temperature in the core is lower than current estimates. But even a moderately small region where protons and neutrons are both superfluid could have an important impact on neutron star precession: for a precession period $P_p(\text{d})$ days the moment of inertia I_p of any region in the core where vortices are pinned to proton flux tubes must be $\lesssim P/P_p \simeq 10^{-5} P(\text{s})/P_p(\text{d})$ times the total moment of inertia of the star (Shaham 1977).

Here, we assume that the magnetic field in the core is strong enough to suppress superconductivity entirely. This means that we suppose that the total magnetic field strength $B = H > H_{c2}$ throughout all of the core. For this to be true, the internal field strength must be at least comparable to and probably larger than the dipole magnetic field at the stellar surface. This may be achieved if there are substantial non-dipolar components of the internal magnetic field, particularly toroidal components (e.g. Cutler 2002). Akgün et al. (2013) found stable, axisymmetric equilibria with toroidal fields $\lesssim 100$ times stronger than the poloidal fields. The deformation due to toroidal fields can be axisymmetric, but if so is *prolate* rather than *oblate*.

Vortex line pinning may also be a problem in the neutron star crust, where neutron pairing is S-wave and superfluid gaps are larger, $\sim \text{MeV}$ (Gezerlis et al. 2014); neutrons are likely to be superfluid down to densities close to neutron drip for temperatures \sim a few $\times 10^8 \text{ K}$ (Potekhin & Chabrier 2018). Unpinning and repinning of neutron superfluid vortices to crustal nuclei have long been thought to be responsible for the behavior of pulsar spins during and after rotational glitches (Anderson & Itoh 1975; Anderson et al. 1982; Alpar et al. 1984; Link et al. 1993). Strong magnetic fields alter the equation of state because the degenerate electron gas becomes one dimensional once

$$\frac{p_F}{m_e c} \lesssim \sqrt{\frac{2eB\hbar}{m_e^2 c^3}} = 6.7 \sqrt{B_{15}} ;$$

the equation of state of the inner crust is largely unaffected for $B \lesssim 10^{17}$ Gauss, although it stiffens considerably in the outer crust (Mutafchieva et al. 2019). The crust ought to crystallize except at low densities for temperatures \lesssim a few $\times 10^9 \text{ K}$ (Carreau et al. 2020). Neutron star precession can only persist in spite of potential pinning of neutron superfluid vortex lines to crustal nuclei or pasta phases (Ravenhall et al. 1983; Hashimoto et al. 1984; Lorenz et al. 1993) if the sustained precession amplitude is large enough (Link & Cutler 2002). The complex topology of the nuclear pasta revealed by molecular dynamics simulations (Schneider et al. 2018) could complicate pinning.

There are two other effects of superstrong crustal magnetic fields that should alter the physical conditions there, perhaps enabling precession to occur. One effect is to shatter the crystalline crust, which can happen if $B^2/8\pi > \mu_{\text{el}}$, where μ_{el} is the elastic shear modulus. Molecular dynamics simulations by Caplan et al. (2018) indicate that the shear modulus of nuclear pasta is $\lesssim 10^{31} \text{ erg cm}^{-3} \equiv (1.6 \times 10^{16} \text{ Gauss})^2/8\pi$, so crustal magnetic fields $\gtrsim 10^{16}$ Gauss would shatter the crust. (See also Pethick & Potekhin 1998).

A second possibility presents itself for magnetic fields larger than the Clogston-Chandrasekhar limiting field strength (Clogston 1962; Chandrasekhar 1962)

$$B_{\text{CC}} = \frac{\Delta_n}{\mu_n \sqrt{2}} \approx 1.2 \times 10^{17} \Delta_n (\text{MeV}) \text{ Gauss} \quad (3)$$

above which flipping the spin of one neutron can break a S-wave Cooper pair; here Δ_n is the neutron gap and μ_n is the neutron magnetic moment. For such large magnetic field strengths, the uniform S-wave BCS superfluid condensate transitions to an inhomogeneous LOFF state (Larkin & Ovchinnikov 1974; Fulde & Ferrell 1964; Kinnunen et al. 2018). Although the implications of such states in the crust have not been explored extensively, it is conceivable that the inhomogeneous LOFF state behaves more like a crystal than a (super)fluid, which may permit precession to occur (Lee et al. 2018). Moreover, somewhat weaker magnetic fields may destroy the predominantly P-wave superfluidity of core neutrons for which $\Delta_n \lesssim 100 \text{ keV}$ (e.g. Haskell & Sedrakian 2018).

In any event, we conclude that magnetic fields stronger than about 10^{16} Gauss are necessary for slow precession. However, the precession period is of order

$$P_p \sim \frac{P}{\epsilon_{\text{mag}}} \sim \frac{100 \text{ d } P(\text{s})}{10^7 \epsilon_{\text{mag}}} \quad (4)$$

which, in view of Eq. (2), suggests a quadrupolar deformation corresponding to $B \sim 10^{14} - 10^{15}$ Gauss for FRB 121102 and FRB 180916.J0158+65, which is too weak to prevent superconductivity of core protons according to Eq. (1). We therefore propose that the magnetic fields inside these magnetars consist of three components:

1. a dipole field with characteristic strength $B_D \sim 10^{14}$ Gauss;
2. a quadrupolar field with characteristic strength $B_T \sim (10^{15} - 10^{16})$ Gauss and a symmetry axis misaligned with the dipole moment;
3. a disordered magnetic field with characteristic strength $B_{\text{turb}} \sim 10^{16}$ Gauss strong enough to suppress superconductivity but with large scale stresses that do not contribute significantly to the quadrupolar deformation of the star.

The spindown timescale in this model is of order

$$t_{\text{sd}} = \frac{I_0 c^3 P^2}{4\pi^2 B_D^2 R^6} \approx \frac{2 \times 10^3 \text{ y } I_{0,45} [P(\text{s})]^2}{B_{D,14}^2 R_{10}^6} \quad (5)$$

where $I_0 = 10^{45} I_{0,45} \text{ gcm}^2$ is the moment of inertia of the star and $B_D = 10^{14} B_{D,14}$ Gauss; the expected ratio of spindown timescale to precession period is

$$\frac{t_{\text{sd}}}{P_p} = \left(\frac{c^3 P}{4\pi^2 GM} \right) \left(\frac{B}{B_D} \right)^2 \left(\frac{I_0}{MR^2} \right) \simeq \frac{7 \times 10^4 P(\text{s})}{M_{1.4}} \left(\frac{B}{10B_D} \right)^2 \left(\frac{I_0}{0.2MR^2} \right) \quad (6)$$

so spindown is very slow compared with precession. Below, we shall also suggest that B_{turb} decays via ambipolar diffusion within $\sim 100 - 1000$ years. That would mean that if FRB 121102 and FRB 180916.J0158+65 have $P \simeq 10$ s they are both younger than their spindown ages and spinning close to their original rotational frequencies. However if they are spinning faster, with $P \simeq 1$ s then they might be about as old as their spindown ages, have quadrupolar distortions $\epsilon_{\text{mag}} \sim 10^{-7}$, and be of order halfway through their lifetimes as precessing neutron stars.

2.2. Magnetic Precession

In this paper, we consider triaxial magnetic distortions that may be far from oblate. We shall see that such configurations lead to qualitatively new features for neutron star precession that may have distinctive observable consequences. Precession of a fluid star caused by magnetic distortions differs qualitatively from solid body precession even though mathematically the two are the same. The inevitability of precession for stars with non-aligned spin and magnetic fields was originally pointed out by Spitzer (1958), and was studied extensively by Mestel and collaborators (Mestel & Takhar 1972; Mestel et al. 1981; Nittmann & Wood 1981). These studies also found that there are slow, internal nonrigid motions in addition to uniform rotation which have been studied recently by Lander & Jones (2017) for neutron stars with toroidal magnetic fields. Below, we neglect these motions, which are second order in small quantities although we recognize that they may be significant for magnetic field evolution.

In a rotating, highly magnetic fluid the matter density is perturbed away from spherical symmetry. The moment of inertia tensor of the star only depends on the $l = 2$ perturbations:

$$I_{ij} = I_0 \left[\delta_{ij} + \epsilon_{\text{rot}} \left(\frac{1}{3} \delta_{ij} - \hat{\Omega}_i \hat{\Omega}_j \right) + \epsilon_{\text{mag}} m_{ij} \right] \quad (7)$$

where rotation is along the $\hat{\Omega}$ direction, ϵ_{rot} and ϵ_{mag} are the amplitudes of the $l = 2$ distortions due to rotation and magnetic fields, respectively, and m_{ij} is symmetric and trace free (STF). The stellar angular momentum is

$$L_i = I_{ij} \Omega_j = I_0 \left[\left(1 - \frac{2\epsilon_{\text{rot}}}{3} \right) \Omega_i + \epsilon_{\text{mag}} m_{ij} \Omega_j \right] \equiv I'_i (\delta_{ij} + \epsilon'_{\text{mag}} m_{ij}) \Omega_j, \quad (8)$$

where we use the summation convention. Since $\epsilon'_{\text{mag}} = \epsilon_{\text{mag}}[1 + \mathcal{O}(\epsilon_{\text{rot}})]$ we ignore the difference between ϵ_{mag} and ϵ'_{mag} below. Invert Eq. (8) to get $\Omega_j = L_i(\delta_{ij} - \epsilon_{\text{mag}}m_{ij})/I'_0$ to first order in small quantities. Since $\epsilon_{\text{mag}}m_{ij}$ is STF

$$\epsilon_{\text{mag}}m_{ij} = -\frac{\epsilon}{2}(\delta_{ij} - \hat{\mathbf{e}}_{3,i}\hat{\mathbf{e}}_{3,j}) + \epsilon\hat{\mathbf{e}}_{3,i}\hat{\mathbf{e}}_{3,j} + \Delta\epsilon(\hat{\mathbf{e}}_{1,i}\hat{\mathbf{e}}_{1,j} - \hat{\mathbf{e}}_{2,i}\hat{\mathbf{e}}_{2,i}); \quad (9)$$

for an axisymmetric magnetic field $\Delta\epsilon = 0$ but we regard this case as exceptional (although Spitzer (1958) and Mestel & Takhar (1972) and subsequent work focused on this situation). Since $\hat{\mathbf{e}}_3$ is fixed in the rotating frame of reference

$$\frac{d\hat{\mathbf{e}}_3}{dt} = \left(1 - \frac{\epsilon}{2}\right) \frac{\mathbf{L} \times \hat{\mathbf{e}}_3}{I'_0} - \frac{\Delta\epsilon(L_1\hat{\mathbf{e}}_2 + L_2\hat{\mathbf{e}}_1)}{I'_0} \Rightarrow \frac{d(\hat{\mathbf{e}}_3 \cdot \mathbf{L})}{dt} = -\frac{2\Delta\epsilon L_1 L_2}{I'_0} \quad (10)$$

in the inertial frame. If the star is axisymmetric, precession is about the magnetic field axis of symmetry, as is well-known (e.g. Spitzer 1958; Goldreich 1970; Mestel & Takhar 1972), but this is untrue for the more general non-axisymmetric case, where precession is more complicated.

For the intense magnetic fields we envision, the main cause of quadrupolar deformations are magnetic stresses. Even in non-barotropic stars, the magnetic field configurations that give rise to *static* deformations are highly constrained (Glampedakis & Lasky 2016). In such a star, the static structure is perturbed away from spherical symmetry by the Lorentz force density \mathbf{f}_L ; to linear order

$$0 = -\nabla\delta P + \hat{\mathbf{r}}g_0(r)\delta\rho - \rho_0(r)\nabla\delta\Psi + \mathbf{f}_L + \mathbf{f}_{NF} \quad (11)$$

where $g_0(r) = -GM(r)/r^2$ is the gravitational acceleration in the unperturbed star, $\delta P(\mathbf{r})$ is the pressure perturbation. \mathbf{f}_{NF} is due to non-fluid forces, and $\delta\Psi$ is the gravitational potential of the perturbation. In the neutron star core, where $\mathbf{f}_{NF} = 0$, axisymmetric static perturbations require that the toroidal field is

$$\mathbf{B}_T = B_T(r, \theta)\hat{\boldsymbol{\varphi}} = \frac{f(\psi)\hat{\boldsymbol{\varphi}}}{r \sin\theta}$$

where $\psi(r, \theta)$ is the flux function of the poloidal field

$$\mathbf{B}_P = \frac{\nabla\psi \times \hat{\boldsymbol{\varphi}}}{r \sin\theta},$$

but for nonaxisymmetric fields $f'(\psi) = \text{constant}$ (Glampedakis & Lasky 2016). Assuming that this restriction holds, Eq. (11) is easy to solve in a non-barotropic star, where δP and $\delta\rho$ are unrelated.

Lasky & Melatos (2013) considered a specific example of a nonaxisymmetric field with dipole and toroidal fields that have different axes of symmetry $\hat{\boldsymbol{\mu}}$ and $\hat{\mathbf{t}}$, respectively, that lead to static deformations of the star. Below, we use a slightly different model for the dipole and toroidal fields, and also include a disordered component. Assuming that the quadrupolar deformation due to the disordered component is relatively small, magnetic forces due to the ordered dipole and toroidal fields result in a perturbed moment of inertia tensor

$$\delta I_{ij} = q_T \left(\frac{\delta_{ij}}{3} - \hat{\mathbf{t}}_i \hat{\mathbf{t}}_j \right) + q_D \left(\hat{\boldsymbol{\mu}}_i \hat{\boldsymbol{\mu}}_j - \frac{\delta_{ij}}{3} \right). \quad (12)$$

Both q_T and q_D are positive, and it follows that the toroidal field promotes prolate deformations relative to a symmetry axis $\hat{\mathbf{t}}$ whereas the dipole field promotes oblate deformations relative to a symmetry axis $\hat{\boldsymbol{\mu}}$. If we assume that

$$\hat{\boldsymbol{\mu}} = \cos\beta\hat{\mathbf{t}} + \sin\beta\hat{\mathbf{u}} \quad (13)$$

in a right-handed $\hat{\mathbf{u}}, \hat{\mathbf{v}}, \hat{\mathbf{t}}$ coordinate system then we find that the eigenvalues of δI_{ij} are

$$\lambda_{\pm} = q_T \left[-\frac{1-d}{6} \pm \sqrt{\left(\frac{1-d}{2}\right)^2 + d\sin^2\beta} \right] \quad \lambda_v = \frac{q_T(1-d)}{3} \quad (14)$$

where we have defined $q_D = dq_T$.

For the dipole field, we adopt a stream function

$$\psi = B_D h(r/R) r^2 [1 - (\hat{\boldsymbol{\mu}} \cdot \hat{\boldsymbol{r}})^2] \quad (15)$$

where the dimensionless function is

$$h(x) = \frac{m(x)}{x^3} \quad (16)$$

for a mass profile $M(r) = Mm(r/R)$. The magnetic field matches smoothly to an exterior vacuum dipole provided that both $\rho = 0$ and $d\rho/dr = 0$ at the stellar surface. Typically, the poloidal magnetic field vanishes somewhere along its equator, and is prone to instability there. In the Cowling approximation we find that

$$q_D = \frac{2\mu^2}{GM} = \frac{2B_D^2 R^6}{GM} \quad [\text{Cowling}] \quad (17)$$

independent of the detailed density profile of the star, but including self-gravity changes q_D by a factor ~ 2 .

The toroidal field must vanish at the surface of the star in order to match to a vacuum exterior. (The toroidal fields in a pulsar magnetosphere are much weaker than the internal toroidal fields we consider here.) For $f'(\psi) = \text{constant}$ in the neutron star core, this important constraint can be satisfied in two ways that lead to very different values of q_T .

1. The toroidal field may fill the core,

$$\mathbf{B}_T = \frac{B_T r h(r/R) \sin \theta \hat{\boldsymbol{\varphi}}}{R} = \frac{B_T m(x) \sin \theta \hat{\boldsymbol{\varphi}}}{x^2} \quad (18)$$

and plunge to zero in a thin boundary region where \mathbf{f}_{NF} may be nonzero, thus loosening constraints on \mathbf{B}_T , even if the crust is damaged severely by its strong magnetic field. The value of q_T depends on the density profile; we adopt

$$\rho(r) = \rho(0) (1 - x^2)^2 \Rightarrow m(x) = \frac{35x^3}{8} - \frac{21x^5}{4} + \frac{15x^7}{8} \text{ and } I_0 = \frac{2MR^2}{9} \quad (19)$$

where I_0 is the moment of inertia of the spherical star; for this particular density profile including self gravity implies

$$q_D \simeq \frac{3.19 B_D^2 R^6}{GM} \Rightarrow \epsilon_{\text{mag},D} \simeq \frac{14.36 B_D^2 R^4}{GM^2}. \quad (20)$$

To zeroth order in the shell thickness

$$q_T = \frac{0.237 B_T^2 R^6}{GM} = \frac{0.188 \langle B_T^2 \rangle R^6}{GM} \Rightarrow \epsilon_{\text{mag},T} = \frac{0.845 B_T^2 R^4}{GM^2} \quad (21)$$

for this model, where $\langle B_T^2 \rangle = 1.26 B_T^2$ is the mean square toroidal field strength. The thin shell contributes about half of the deformation, which may be unrealistic, so actual values could be as small as half as large.

2. The toroidal field may be confined to a limited volume if instead of Eq. (18)

$$\mathbf{B}_T = B_T \hat{\boldsymbol{\varphi}} \left[\frac{m(x) \sin \theta}{x^2} - \frac{1}{x \sin \theta} \right] \Theta \left(\frac{m(x) \sin \theta}{x^2} - \frac{1}{x \sin \theta} \right), \quad (22)$$

which is the model used by [Lasky & Melatos \(2013\)](#). (See also [Akgün et al. \(2013\)](#), who introduced models of this type in their study of magnetic stability in axisymmetry.) The field only occupies about 21% of the stellar volume, and has a mean square $\langle B_T^2 \rangle = 0.01 B_T^2$ within this volume. In this case

$$q_T = \frac{3.53 \times 10^{-4} B_T^2 R^6}{GM} = \frac{3.53 \times 10^{-2} \langle B_T^2 \rangle R^6}{GM} \Rightarrow \epsilon_{\text{mag},T} = \frac{1.59 \times 10^{-1} \langle B_T^2 \rangle R^4}{GM^2}. \quad (23)$$

The quadrupole moment for this model is diminished severely because it is confined to such a small volume.

3. Interpreting these two models as extremes for quadrupolar distortion due to toroidal fields we estimate

$$q_T \simeq \frac{(0.04 - 0.2) \langle B_T^2 \rangle R^6}{GM} \quad (24)$$

and therefore

$$d = \frac{q_D}{q_T} \simeq \frac{(20 - 100)B_D^2}{\langle B_T^2 \rangle} = \frac{(0.2 - 1)(10B_D)^2}{\langle B_T^2 \rangle}. \quad (25)$$

Thus, $d \lesssim 1$ and may even be $\ll 1$; the quadrupolar distortions arising from ordered field are significantly triaxial, and very likely prolate.

If the toroidal field occupies a small volume, as for Eq. (22), then no matter how large $\langle B_T^2 \rangle$ is the field will be incapable of suppressing proton superconductivity everywhere. Even if the field occupies much of the star, as in Eq. (18), it may not be strong enough to exceed H_{c2} even if it is much stronger than B_D . Moreover, as noted above \mathbf{B}_P is prone to instability in this model. Although the toroidal field represented by Eq. (22) can prevent the instability in axisymmetry if $\langle B_T^2 \rangle$ is large enough (Akgün et al. 2013) we doubt that the tilted dipole model is stable ($\nabla \times \mathbf{B}_T \parallel \mathbf{B}_P$ for both Eqs. (22) and (18) in axisymmetry but not in the tilted dipole model.) For these reasons we conclude that a precessing neutron star with internal fields that are stable on short timescales ought to include a disordered component for with characteristic local field strength $B_{\text{turb}} > \sqrt{\langle B_T^2 \rangle} > B_D$. The disordered field may be a remnant of the violent process that generated the strong internal magnetic fields (Thompson & Duncan 1993; Braithwaite 2009).

The turbulent magnetic field is

$$\mathbf{B}_{\text{turb}} = \nabla N_1(\mathbf{x}) \times \nabla N_2(\mathbf{x}) \quad (26)$$

where the scalar functions $N_i(\mathbf{x})$ are constant along field lines and are advected with the fluid in the limit of perfect conductivity. We can think of N_i as a pair of comoving field line labels. We assume that the turbulence is small scale locally but with a large scale bias, so that we can expand

$$N_i(\mathbf{x}) = \frac{1}{\sqrt{V}} \sum_{\mathbf{k}} S_i(\epsilon \mathbf{x}, k) \exp[i(\mathbf{k} \cdot \mathbf{x}) + i\psi_i(\mathbf{k})] \quad (27)$$

where $S_i(\epsilon \mathbf{x}, k)$ is a spectral function and ϵ is the ratio of the small scale that characterizes the local turbulence and the large scale that characterizes the bias; V is a normalization volume and $\psi_i(\mathbf{k})$ is a random phase. If we assume that $\psi_1(\mathbf{k}) = \psi_2(\mathbf{k})$, which is plausible if the turbulent field results from fluid motions that stretch, twist and fold individual field lines, then Eq. (26) has a mean value $\sim \epsilon^2$ times the characteristic local field amplitude, and there are magnetic forces $\sim \epsilon$ (corresponding to gradient of turbulent magnetic pressure), $\sim \epsilon^3$ and $\sim \epsilon^5$ (corresponding to the mean field). We assume that the local field is strong enough to destroy superconductivity, but that the forces are too weak to have much effect on quadrupolar deformation. However, we do hope that the stresses can act as *deus ex machina* to stabilize the ordered fields.

Magnetic fields in the core of a highly magnetic neutron star containing normal neutrons and protons decay via ambipolar diffusion: Reisenegger & Goldreich (1992) estimate a decay timescale

$$t_{\text{ambip}}(L) \sim \frac{220 \text{ y} (20Y)(T_8/3)^2 [L(\text{km})]^2 (n_b/n_{\text{nuc}})^{2/3}}{B_{16}^2(L)}, \quad (28)$$

for field varying on a length scale $L(\text{km})$ km, where n_b is baryon density, $n_{\text{nuc}} = 0.16 \text{ fm}^{-3}$ is nuclear density, Yn_b is the proton density, and $T = 10^8 T_8$. (See also Glampedakis et al. (2011), Passamonti et al. (2017) and Gusakov et al. (2017), Fig. 1.) Neutron superfluidity would increase the decay time but as long as the core temperature is as high as \sim a few $\times 10^8$ K the normal neutron fraction will be considerable in much of the core, and Eq. (28) remains true within a factor of an order of magnitude or less. (Field decay heats the core, but given the steep T dependence of neutrino cooling the core temperature is not changed substantially.) The tangled component will decay on a timescale that depends on its fluctuation spectrum: if $B^2(L) \propto L^\alpha$ the decay timescale $t_{\text{ambip}}(L) \propto L^{2-\alpha}$, which implies faster decay on smaller scales for $\alpha < 2$ and vice-versa; theories of fully developed magnetic turbulence generally find $\alpha < 1$ (Iroshnikov 1963; Kraichnan 1965; Goldreich & Sridhar 1995). Plausibly, the tangled field decays away in a time $\lesssim 10^3$ y, after which substantial portions of the magnetar core become superconducting, which limits the time span during which a magnetar may precess slowly. The larger scale ordered fields also decay as long as core protons are normal but since $L(\text{km}) \simeq 10$ for these fields they may survive relatively undiminished until protons become superconducting, after which ambipolar diffusion becomes ineffective. Ambipolar diffusion in the crust is suppressed by neutron superfluidity. Magnetic field evolution in a magnetar crust involves an interplay among the Hall effect, Ohmic dissipation and plastic flow (Lander & Gourgouliatos 2019; Li et al. 2016), involving instabilities on timescales $\sim 10^3$ y (Gourgouliatos &

Pons 2020) and possibly evolution toward an attractor solution on timescales $\sim 10^5$ y (Gourgouliatos & Cumming 2014b,a). (The effect of Landau quantization of crustal electrons on magnetar magnetic field evolution, which may be substantial, is being included for the first time in a forthcoming paper by Rau, P. B. & Wasserman (2021).)

2.3. Triaxial Precession

Conservation of angular momentum is

$$\frac{d\mathbf{L}}{dt} = \frac{d^*\mathbf{L}}{dt} + \boldsymbol{\Omega} \times \mathbf{L} = \mathbf{N} \quad (29)$$

where \mathbf{L} is the angular momentum and \mathbf{N} is the spindown torque; d^*/dt is time derivative in rotating frame. Substitute $\mathbf{L} = L\hat{\boldsymbol{\ell}}$ where $L = |\mathbf{L}|$ to get

$$\frac{dL}{dt} = \frac{d^*L}{dt} = \hat{\boldsymbol{\ell}} \cdot \mathbf{N} \equiv N_{\parallel}, \quad (30)$$

and

$$\frac{d^*\hat{\boldsymbol{\ell}}}{dt} + \boldsymbol{\Omega} \times \hat{\boldsymbol{\ell}} = \frac{\mathbf{N} - \hat{\boldsymbol{\ell}}\hat{\boldsymbol{\ell}} \cdot \mathbf{N}}{L} \equiv \frac{\mathbf{N}_{\perp}}{L}. \quad (31)$$

For the spindown torque we adopt

$$\mathbf{N} = -\frac{k\mu^2\Omega^2}{c^3}(\boldsymbol{\Omega} - a\boldsymbol{\Omega} \cdot \hat{\boldsymbol{\mu}}\hat{\boldsymbol{\mu}}) \Rightarrow N_{\parallel} = -\frac{k\mu^2\Omega^2}{c^3}(\hat{\boldsymbol{\ell}} \cdot \boldsymbol{\Omega} - a\boldsymbol{\Omega} \cdot \hat{\boldsymbol{\mu}}\hat{\boldsymbol{\mu}}) \quad (32)$$

where $\boldsymbol{\mu}$ is the magnetic moment of the star, k and a are numerical constants ~ 1 ; for numerical evaluations we adopt $k = 2$ and $a = 1/2$, which corresponds to a rate of energy loss $\boldsymbol{\Omega} \cdot \mathbf{N} = (\mu^2\Omega^4/c^3)(1 + \sin^2\theta)$ where $\cos\theta = \hat{\boldsymbol{\Omega}} \cdot \hat{\boldsymbol{\mu}}$ (Li et al. 2012). (The same spindown model was used in Akgün et al. (2006).) The angular velocity of rotation is

$$\boldsymbol{\Omega} = L \left(\frac{\hat{\boldsymbol{e}}_1\hat{\boldsymbol{\ell}}_1}{I_1} + \frac{\hat{\boldsymbol{e}}_2\hat{\boldsymbol{\ell}}_2}{I_2} + \frac{\hat{\boldsymbol{e}}_3\hat{\boldsymbol{\ell}}_3}{I_3} \right) = \frac{L}{I_3} \left[\frac{I_3\hat{\boldsymbol{e}}_1\hat{\boldsymbol{\ell}}_1}{I_1} + \frac{I_3\hat{\boldsymbol{e}}_2\hat{\boldsymbol{\ell}}_2}{I_2} + \hat{\boldsymbol{e}}_3\hat{\boldsymbol{\ell}}_3 \right] \quad (33)$$

where $I_3 > I_2 > I_1$ are the moments of inertia along the principal axes of the quadrupolar distortion; we define a parameter $0 < e^2 < \infty$, which measures the degree of triaxiality, in terms of which

$$\frac{I_3}{I_2} = 1 + \frac{2\epsilon_{\text{mag}}}{2+e^2}, \quad \frac{I_3}{I_1} = 1 + \frac{2(1+e^2)\epsilon_{\text{mag}}}{2+e^2}, \quad e^2 = \frac{I_3(I_2 - I_1)}{I_1(I_3 - I_2)} \quad (34)$$

where ϵ_{mag} is given by Eq. (2). Oblate axisymmetric distortions ($I_1 = I_2$) correspond to $e^2 = 0$; prolate axisymmetric distortions ($I_3 = I_2$) correspond to $e^2 \rightarrow \infty$. For the tilted dipole model (see Eq. (14) and Lasky & Melatos 2013)

$$e^2 = \frac{I_3(|1-d|\sqrt{1+\Delta}+1-d)}{I_1(|1-d|\sqrt{1+\Delta}-(1-d))}, \quad \Delta = \frac{4d\sin^2\beta}{(1-d)^2}. \quad (35)$$

For $d \gg 1 \Rightarrow \Delta \simeq 4\sin^2\beta/d \ll 1$ the dipole field dominates the quadrupolar distortion and Eq. (35) implies that $e^2 \simeq \Delta/4 \simeq \sin^2\beta/d \ll 1$. For $d \ll 1 \Rightarrow \Delta \simeq 4d\sin^2\beta \ll 1$ the toroidal field dominates the quadrupolar distortion, and Eq. (35) implies that $e^2 \simeq 4/\Delta = 1/d\sin^2\beta \gg 1$. For $\beta = 0$, the axisymmetric case, $e^2 = 0$ if $d > 1$ and $e^2 = \infty$ for $d < 1$.

The Euler equations have an exact conservation law

$$\hat{\boldsymbol{\ell}}_1^2 + \hat{\boldsymbol{\ell}}_2^2 + \hat{\boldsymbol{\ell}}_3^2 = 1 \quad (36)$$

because $\hat{\boldsymbol{\ell}}$ is a unit vector, but there is also an approximate conservation law

$$\boldsymbol{\Omega} \cdot \hat{\boldsymbol{\ell}} = \frac{\hat{\boldsymbol{\ell}}_1^2}{I_1} + \frac{\hat{\boldsymbol{\ell}}_2^2}{I_2} + \frac{\hat{\boldsymbol{\ell}}_3^2}{I_3} \equiv \frac{2E_{\text{rot}}}{L_0^2}; \quad (37)$$

$d^*(\boldsymbol{\Omega} \cdot \hat{\boldsymbol{\ell}})/dt = -\boldsymbol{\Omega} \cdot \mathbf{N}_{\perp}$ so $\boldsymbol{\Omega} \cdot \hat{\boldsymbol{\ell}}$ only varies appreciably on a timescale of order $1/\epsilon_{\text{mag}}$ times the spindown time. In Eq. (37) the parameter L_0 is the magnitude of the stellar angular momentum at some reference start time, which could be the time when precession is excited.

The Euler equations allow steady state rotation about any of its three principal axes. By combining Eqs. (36) and (37) in three different ways appropriate to perturbation away from each principal axis we find

$$\begin{aligned}\frac{E_{\text{rot}}}{L_0^2/2I_3} - 1 &= \frac{2\epsilon_{\text{mag}}[\hat{\ell}_1^2(1+e^2) + \hat{\ell}_2^2]}{2+e^2} \\ \frac{E_{\text{rot}}}{L_0^2/2I_2} - 1 &= \frac{2\epsilon_{\text{mag}}(\hat{\ell}_1^2 e^2 - \hat{\ell}_3^2)}{2+e^2 + 2\epsilon_{\text{mag}}} \\ \frac{E_{\text{rot}}}{L_0^2/2I_1} - 1 &= -\frac{2\epsilon_{\text{mag}}[\hat{\ell}_2^2 e^2 + \hat{\ell}_3^2(1+e^2)]}{2+e^2 + 2\epsilon_{\text{mag}}(1+e^2)}.\end{aligned}\quad (38)$$

Eq. (38) shows that at a given angular momentum, the lowest energy state is rotation about \hat{e}_3 , the highest is rotation about \hat{e}_1 and rotation about \hat{e}_2 is intermediate, as is well-known. For axisymmetric oblate precession ($e^2 = 0$) the \hat{e}_1 and \hat{e}_2 directions are interchangeable, and precession about either one is unstable but stable about the symmetry axis \hat{e}_3 , but for axisymmetric prolate precession ($e^2 \rightarrow \infty$) the \hat{e}_2 and \hat{e}_3 directions are interchangeable, and precession is stable about either one and unstable about the symmetry axis \hat{e}_1 .

Below, we will use the first of Eqs. (38) to quantify the second conservation law by defining the energy perturbation above the minimum energy state to be

$$E_{\text{rot}} = \frac{L_0^2}{2I_3} \left[1 + \frac{2\epsilon_{\text{mag}}\Lambda^2(1+e^2)}{2+e^2} \right] \Rightarrow \delta E_p = E_{\text{rot}} - \frac{L_0^2}{2I_3} = \frac{L_0^2\Lambda^2\epsilon_{\text{mag}}(1+e^2)}{I_3(2+e^2)}, \quad (39)$$

where δE_p is the extra energy associated with precession. Using Eq. (39) we write the conservation law as

$$\Lambda^2(1+e^2) = \hat{\ell}_1^2(1+e^2) + \hat{\ell}_2^2. \quad (40)$$

Suppose precession is excited from its minimum energy state by injection of rotational energy $\delta E_p = \eta L_0^2/2I_3$. This is consistent with exciting precession with amplitude

$$\Lambda^2(1+e^2) = \frac{(2+e^2)\eta}{2\epsilon_{\text{mag}}} \equiv \frac{\eta}{\eta_{\text{crit}}} \quad \eta_{\text{crit}} = \frac{2\epsilon_{\text{mag}}}{2+e^2}. \quad (41)$$

There are then two very different cases depending on how much energy is injected: if $\eta < \eta_{\text{crit}}$ then $\Lambda^2(1+e^2) < 1$ and if $\eta > \eta_{\text{crit}}$ then $\Lambda^2(1+e^2) > 1$. We shall treat each of these cases, which have very different properties, separately. Qualitatively, we shall see that $\Lambda^2(1+e^2) < 1$ has well defined $e^2 \rightarrow 0$ (axisymmetric, oblate) limiting dynamics whereas $\Lambda^2(1+e^2) > 1$ has well defined $e^2 \rightarrow \infty$ (axisymmetric, prolate) limiting dynamics. Since $\epsilon_{\text{mag}} \simeq \beta_2 E_{\text{mag}}/E_\star$

$$\epsilon_{\text{mag}} \simeq \frac{\beta_2 E_{\text{mag}}}{E_\star} \quad (42)$$

where $E_{\text{mag}} \sim B^2 R^3$ is the magnetic energy and $E_\star \sim GM^2/R$ is the binding energy of the neutron star, a more apt comparison is

$$\frac{\delta E_p}{E_{\text{mag}}} \simeq \frac{2\beta_2\epsilon_{\text{rot}}(1+e^2)\Lambda^2}{2+e^2} \quad (43)$$

where $\epsilon_{\text{rot}} = L^2/2I_3 E_\star$ is the rotational distortion of the star.

For a rotation period ~ 1 second we expect $\epsilon_{\text{rot}} \sim I\Omega^2 R/GM^2 \sim 10^{-7} I_{45} R_{10}^3/M_{1.4}[P(\text{s})]^2$ so the energy required to excite even high amplitude precession is only a small fraction of the magnetic energy of the star. Even small changes in the magnetic field can engender relatively large amplitude precession. To make this quantitative, suppose that a shearing event in the neutron star distorts the magnetic field changing the moment of inertia of the star from \mathbf{I} to $\mathbf{I}' = \mathbf{I} + \Delta\mathbf{I}$, where $\Delta\mathbf{I}$ is STF. The eigenvalues of \mathbf{I}' are slightly different than those of \mathbf{I} , and its eigenvectors are rotated relative to the eigenvectors of \mathbf{I} . If the eigenvalues and associated eigenvectors of \mathbf{I} are (I_i, \hat{e}_i) , then to lowest order in $\|\Delta\mathbf{I}\|$ the eigenvalues and eigenvectors of \mathbf{I}' are

$$I'_i = I_i + \Delta I_{ii} \quad \hat{e}'_i \simeq \hat{e}_i \left(1 - \frac{1}{2} \sum_{j \neq i} \theta_{ij}^2 \right) + \sum_{j \neq i} \theta_{ij} \hat{e}_j \quad \theta_{ij} = \frac{\Delta I_{ij}}{I'_i - I'_j}, \quad (44)$$

normalizing the eigenvectors so that $\hat{\mathbf{e}}'_i \cdot \hat{\mathbf{e}}'_j = \delta_{ij}$. Since we expect $\Delta I_{ij} = s_{ij} \epsilon_{\text{mag}}$, where s_{ij} is STF with magnitude $\lesssim 1$, and $|I'_i - I'_j| \sim \epsilon_{\text{mag}}$ the rotations involve angles $\lesssim 1$, not $\sim \epsilon_{\text{mag}} \ll 1$. Assuming that \mathbf{L} is conserved in the shearing event, its projection along the rotated principal axes of \mathbf{I}' differs from its projection along \mathbf{I} . For example, suppose that the star was rotating without any precession at all along $\hat{\mathbf{e}}_3$, the axis of largest moment of inertia, prior to the shearing event; then afterwards

$$\hat{\boldsymbol{\ell}} \simeq \hat{\mathbf{e}}'_1 \theta_{13} + \hat{\mathbf{e}}'_2 \theta_{23} + \hat{\mathbf{e}}'_3 \left[1 - \frac{1}{2} (\theta_{13}^2 + \theta_{23}^2) \right] , \quad (45)$$

and the star will precess. If angular momentum is conserved as the field rearranges itself, then the angular velocity changes during the shearing event by

$$\Delta \Omega_i = - \frac{\Delta I_{ij} \Omega_j}{I_i}$$

working in the reference frame where \mathbf{I} is diagonal. The associated change in rotational energy is

$$\Delta E_{\text{rot}} = L_i \Delta \Omega_i = - \frac{L_i \Delta I_{ij} \Omega_j}{I_i} = - \Omega_i \Delta I_{ij} \Omega_j = - \epsilon_{\text{mag}} \Omega_i s_{ij} \Omega_j . \quad (46)$$

ΔE_{rot} might be negative or positive, and is not equal to the extra energy in precession above the minimum energy state corresponding to rotation about $\hat{\mathbf{e}}'_3$, in part because the magnitude of the angular velocity changes as a result of the shearing event. In rough order of magnitude $|\delta E_{\text{rot}}| \lesssim \epsilon_{\text{rot}} E_{\text{mag}}$.

Phenomena associated with the spindown torque include a cyclical variation over a precession cycle and a secular torque that develops very slowly compared with the precession period. We discuss these in Sections 2.4 and 2.5 using a perturbative technique similar to Goldreich (1970) but generalized to triaxial precession. To zeroth order, we neglect spindown effects, and Eq. (31) becomes

$$\frac{d\hat{\boldsymbol{\ell}}_1}{d\phi} = - \frac{2\epsilon_{\text{mag}} \hat{\boldsymbol{\ell}}_2 \hat{\boldsymbol{\ell}}_3}{2 + e^2} \quad \frac{d\hat{\boldsymbol{\ell}}_2}{d\phi} = \frac{2\epsilon_{\text{mag}} \hat{\boldsymbol{\ell}}_1 \hat{\boldsymbol{\ell}}_3 (1 + e^2)}{2 + e^2} \quad \frac{d\hat{\boldsymbol{\ell}}_3}{d\phi} = - \frac{2\epsilon_{\text{mag}} \hat{\boldsymbol{\ell}}_1 \hat{\boldsymbol{\ell}}_2 e^2}{2 + e^2} \quad (47)$$

where $d\phi = (L/I_3)dt$ is differential spin phase.

From an observational standpoint, we are most interested in the motion of the direction from the star to the observer, $\hat{\mathbf{n}}$, in the rotating frame of reference. In the inertial frame, where $\hat{\boldsymbol{\ell}}$ is independent of time to lowest order, let

$$\hat{\mathbf{n}} = \cos i \hat{\boldsymbol{\ell}} + \sin i \hat{\mathbf{e}}_x . \quad (48)$$

To project $\hat{\mathbf{n}}$ into the rotating frame we use a standard Euler angle rotation (Gottfried 1966): (i) Rotate angle $\alpha \in [0, 2\pi]$ about the 3 axis to get new axes $1', 2', 3' = 3$, (ii) Rotate angle $\beta \in [0, \pi]$ about the $2'$ axis to get new axes $1'', 2'' = 2', 3'' = z$. (iii) Rotate angle $\gamma \in [0, 2\pi]$ about the $3'' = z$ axis to get the axes x, y, z . In terms of the angles α, β and γ we get $\hat{\mathbf{n}} = \hat{n}_i \hat{\mathbf{e}}_i$ where

$$\begin{aligned} \hat{n}_1 &= \sin i (\cos \alpha \cos \beta \cos \gamma - \sin \alpha \sin \gamma) - \cos i \cos \alpha \sin \beta \\ \hat{n}_2 &= \sin i (\sin \alpha \cos \beta \cos \gamma + \cos \alpha \sin \gamma) - \cos i \sin \alpha \sin \beta \\ \hat{n}_3 &= \sin i \cos \gamma \sin \beta + \cos i \cos \beta . \end{aligned} \quad (49)$$

If we define $\hat{\boldsymbol{\ell}} = \hat{\mathbf{z}}$ in the inertial frame we find that $\cos \beta = \hat{\boldsymbol{\ell}}_3$ and

$$\sin \alpha = - \frac{\hat{\boldsymbol{\ell}}_2}{\sqrt{\hat{\boldsymbol{\ell}}_1^2 + \hat{\boldsymbol{\ell}}_2^2}} \quad \cos \alpha = - \frac{\hat{\boldsymbol{\ell}}_1}{\sqrt{\hat{\boldsymbol{\ell}}_1^2 + \hat{\boldsymbol{\ell}}_2^2}} . \quad (50)$$

Using $d\hat{\mathbf{e}}_i/dt = \boldsymbol{\Omega} \times \hat{\mathbf{e}}_i$ for any of the principal axes we find that

$$\frac{d\gamma}{d\phi} = -1 - \frac{2\epsilon_{\text{mag}} [(1 + e^2) \hat{\boldsymbol{\ell}}_1^2 + \hat{\boldsymbol{\ell}}_2^2]}{(2 + e^2)(\hat{\boldsymbol{\ell}}_1^2 + \hat{\boldsymbol{\ell}}_2^2)} = -1 - \frac{2\epsilon_{\text{mag}} \Lambda^2 (1 + e^2)}{(2 + e^2)(\hat{\boldsymbol{\ell}}_1^2 + \hat{\boldsymbol{\ell}}_2^2)} \quad (51)$$

using Eq. (40). Note that these results can be used for both $\Lambda \sqrt{1 + e^2} < 1$ and $\Lambda \sqrt{1 + e^2} > 1$.

In the rotating frame of reference, $\hat{\mathbf{n}} = \cos i \hat{\boldsymbol{\ell}} + \sin i (\hat{\mathbf{e}}_a \cos \gamma + \hat{\mathbf{e}}_b \sin \gamma)$ where $\hat{\mathbf{e}}_a = (\hat{\boldsymbol{\ell}} \times \hat{\mathbf{e}}_3) \times \hat{\boldsymbol{\ell}} / \sin \beta$ and $\hat{\mathbf{e}}_b = \hat{\boldsymbol{\ell}} \times \hat{\mathbf{e}}_3 / \sin \beta$ are slowly varying unit vectors perpendicular to $\hat{\boldsymbol{\ell}}$; $\hat{\mathbf{n}}$ rotates rapidly in the retrograde direction in the plane instantaneously perpendicular to $\hat{\boldsymbol{\ell}}$. For emission along a beam direction $\hat{\mathbf{b}}$ the observed intensity depends on

$$\hat{\mathbf{b}} \cdot \hat{\mathbf{n}} = \cos i \hat{\mathbf{b}} \cdot \hat{\boldsymbol{\ell}} + \sin i \left(\hat{\mathbf{b}} \cdot \hat{\mathbf{e}}_a \cos \gamma + \hat{\mathbf{b}} \cdot \hat{\mathbf{e}}_b \sin \gamma \right) .$$

Define $\hat{\mathbf{b}} \cdot \hat{\boldsymbol{\ell}} = \cos \eta_b$, $\hat{\mathbf{b}} \cdot \hat{\mathbf{e}}_a = \sin \eta_b \cos \psi_b$ and $\hat{\mathbf{b}} \cdot \hat{\mathbf{e}}_b = \sin \eta_b \sin \psi_b$; then

$$\hat{\mathbf{b}} \cdot \hat{\mathbf{n}} = \cos i \cos \eta_b + \sin i \sin \eta_b \cos(\gamma - \psi_b) , \quad (52)$$

where η_b and ψ_b vary during the precession cycle for a given $\hat{\mathbf{b}}$.

For ‘‘pulsar-like’’ behavior, beam directions are randomly distributed in a narrow cone around a dominant direction. Given unlimited sensitivity, the observed intensity would be nearly periodic, with periodic timing residuals due to precession $\lesssim 1$ radian of spin phase. The amplitude of the rapidly oscillating term in Eq. (52) is $\propto \sin \eta_b$, which varies during the precession cycle. Presumably the observed intensity is a decreasing function of $\hat{\mathbf{b}} \cdot \hat{\mathbf{n}}$, so the observed intensity has extrema when

$$\frac{d\hat{\mathbf{b}} \cdot \hat{\mathbf{n}}}{d\phi} = 0 , \quad (53)$$

which has solutions twice per cycle, only one of which corresponds to the maximum value of $\hat{\mathbf{b}} \cdot \hat{\mathbf{n}}$. Intrinsic intensity fluctuations and imperfect, time-varying and often unfavorable beaming due to precession turn out to render most pulses undetectable, but nevertheless the spin frequency would be discernible readily in this case.

For ‘‘stochastic behavior’’ in which outbursts occur randomly in time with a random distribution of beam directions it is much harder but not impossible to uncover the pulse frequency. If the beams emit into narrow cones, Eq. (52) implies that most outbursts will not be seen but there will be a bias favoring times when $\hat{\mathbf{b}} \cdot \hat{\mathbf{n}}$ is near one. This bias imprints the effect of fast rotation on the times when outbursts happen, but only weakly, so the spin frequency is only discernible after many bursts have been detected. We develop a specific model for stochastic outbursts in §3. An approximate analytic model that elucidates how information about the spin frequency and precession period is imprinted on the modelled series of burst detection times may be found in Appendix B.

Intermediate between these two extreme models would be one in which FRBs occur randomly in time but are triggered by exceptionally narrow beams within a restricted range of possible directions. For an outburst occurring at a particular time, the associated FRB would only be seen if $\hat{\mathbf{b}}$ is very nearly parallel to $\hat{\mathbf{n}}$, as determined from Eqs. (49) with Eq. (50), and $\hat{\mathbf{n}}$ is in the range of allowed beam directions.

Table 1 details the solutions of the Euler equations. Note that the solutions are continuous across the limiting case $\Lambda\sqrt{1+e^2} = 1 = q$, but because the precession period diverges logarithmically as $q \rightarrow 1$ (from either side) the solutions are not really connected physically across $q = 1$.

There are two different axisymmetric situations, $e^2 = 0$, which is oblate ($I_1 = I_2 < I_3$), and $e^2 = \infty$, which is prolate ($I_3 = I_2 > I_1$); these solutions are listed in Table 1. However, these are singular limiting cases: $q = e\Lambda/\sqrt{1-\Lambda^2}$ is identically zero for $e = 0$ and any value of $\Lambda \neq 1$ and is infinity for $e = \infty$ for any value of $\Lambda \neq 0$.

The ratio of the neutron star spin period P to its precession period P_p is

$$\frac{P}{P_p} = \frac{2\pi}{\phi_{p,\text{cyc}}} = \frac{\pi\epsilon_{\text{mag}}e\Lambda\sqrt{1+e^2}}{2+e^2} \begin{cases} 1/qF(\pi/2|q) & [q < 1] \\ 1/F(\pi/2|1/q) & [q > 1] \end{cases} \quad (54)$$

which is plotted in Fig. 1 for various values of e^2 as a function of $\Lambda\sqrt{1+e^2}$. The smallest values of $P/P_p\epsilon_{\text{mag}}$ are for $\Lambda\sqrt{1+e^2} < 1$ and large e^2 , except for the region right around $\Lambda\sqrt{1+e^2} = 1$, where $P/\epsilon_{\text{mag}}P_p \rightarrow 0$ for all values of e^2 . Since R1 and R3 both have very long P_p , Fig. 1 favors models with large values of e^2 , which implies that the toroidal component of magnetic field is significantly larger than the poloidal component, unless the star is fortuitously close to $\Lambda\sqrt{1+e^2} = 1$.

2.4. Periodic Timing Residuals from Precession Plus Spindown

Here, we derive the equation for $t(\phi)$, the functional dependence of time on spin phase, which we have defined previously as $d\phi = (L/I_3)dt$; we use Eqs. 30 and 32 to zeroth order in ϵ_{mag} to get

$$\frac{d\Omega}{d\phi} = -\frac{k\mu^2\Omega^2[1-a(\hat{\boldsymbol{\mu}} \cdot \hat{\boldsymbol{\ell}})^2]}{Ic^3} \Rightarrow \frac{d}{d\phi} \left(\frac{1}{\Omega} \right) = \frac{d^2t}{d\phi^2} = \frac{k\mu^2[1-a(\hat{\boldsymbol{\mu}} \cdot \hat{\boldsymbol{\ell}})^2]}{Ic^3} \quad (55)$$

Table 1. Precession Solutions

	$0 < \Lambda\sqrt{1+e^2} < 1$	$1 < \Lambda\sqrt{1+e^2} < \sqrt{1+e^{2a}}$
q	$\frac{e\Lambda}{\sqrt{1-\Lambda^2}} < 1$	$\frac{e\Lambda}{\sqrt{1-\Lambda^2}} > 1$
Φ^b	$F(\varphi(\Phi) q) = \int_0^{\varphi(\Phi)} \frac{d\varphi'}{\sqrt{1-q^2 \sin^2 \varphi'}}$	$F(\varphi(\Phi) 1/q) = \int_0^{\varphi(\Phi)} \frac{d\varphi'}{\sqrt{1-\sin^2 \varphi'/q^2}}$
$\text{sn}\Phi$	$\sin[\varphi(\Phi)]$	$\sin[\varphi(\Phi)]$
$\text{cn}\Phi$	$\cos[\varphi(\Phi)]$	$\cos[\varphi(\Phi)]$
$\text{dn}\Phi$	$\sqrt{1-q^2 \text{sn}^2\Phi}$	$\sqrt{1-\text{sn}^2\Phi/q^2}$
$\Phi_{p,\text{cyc}}^c$	$4F(\pi/2 q)$	$4F(\pi/2 1/q)$
$d\Phi/d\phi$	$\frac{2\epsilon_{\text{mag}}\sqrt{(1-\Lambda^2)(1+e^2)}}{2+e^2} = \frac{2\epsilon_{\text{mag}}e\Lambda\sqrt{1+e^2}}{q(2+e^2)}$	$\frac{2\epsilon_{\text{mag}}e\Lambda\sqrt{1+e^2}}{2+e^2} = \frac{2\epsilon_{\text{mag}}q\sqrt{(1-\Lambda^2)(1+e^2)}}{2+e^2}$
$\phi_{p,\text{cyc}}^d$	$\frac{2(2+e^2)F(\pi/2 q)}{\epsilon_{\text{mag}}\sqrt{(1-\Lambda^2)(1+e^2)}} = \frac{2q(2+e^2)F(\pi/2 q)}{\epsilon_{\text{mag}}e\Lambda\sqrt{1+e^2}}$	$\frac{2(2+e^2)F(\pi/2 1/q)}{\epsilon_{\text{mag}}e\Lambda\sqrt{1+e^2}} = \frac{2(2+e^2)F(\pi/2 1/q)}{\epsilon_{\text{mag}}q\sqrt{(1-\Lambda^2)(1+e^2)}}$
$\hat{\ell}_1$	$\Lambda \text{cn}\Phi$	$\Lambda \text{dn}\Phi$
$\hat{\ell}_2$	$\Lambda\sqrt{1+e^2} \text{sn}\Phi$	$\frac{\sqrt{(1-\Lambda^2)(1+e^2)} \text{sn}\Phi}{e} = \frac{\Lambda\sqrt{1+e^2} \text{sn}\Phi}{q}$
$\hat{\ell}_3$	$\sqrt{1-\Lambda^2} \text{dn}\Phi$	$\sqrt{1-\Lambda^2} \text{cn}\Phi$
$1 + \frac{d\gamma}{d\phi}$	$-\frac{\sqrt{1+e^2}d\Phi/d\phi}{\sqrt{(1-\Lambda^2)(1+e^2 \text{sn}^2\Phi)}} = -\frac{q\sqrt{1+e^2}d\Phi/d\phi}{e\Lambda(1+e^2 \text{sn}^2\phi)}$	$-\frac{\Lambda\sqrt{1+e^2}d\Phi/d\phi}{e[\Lambda^2+(1-\Lambda^2)\text{sn}^2\Phi]} = -\frac{\sqrt{1+e^2}d\Phi/d\phi}{e\Lambda(1+e^2 \text{sn}^2\Phi/q^2)}$ $= -\frac{\sqrt{1+e^2}d\Phi/d\phi}{q\sqrt{1-\Lambda^2}(1+e^2 \text{sn}^2\Phi/q^2)}$
	$e^2 = 0.0$ (Axisymmetric, Oblate)	$e^2 = \infty$ (Axisymmetric, Prolate)
$d\Phi/d\phi$	$\epsilon_{\text{mag}}\sqrt{1-\Lambda^2}$	$2\epsilon_{\text{mag}}\Lambda$
$\hat{\ell}_1$	$\Lambda \cos \Phi$	Λ
$\hat{\ell}_2$	$\Lambda \sin \Phi$	$\sqrt{1-\Lambda^2} \sin \Phi$
$\hat{\ell}_3$	$\sqrt{1-\Lambda^2}$	$\sqrt{1-\Lambda^2} \cos \Phi$
$1 + \frac{d\gamma}{d\phi}$	$-\frac{d\Phi/d\phi}{\sqrt{1-\Lambda^2}} = -\epsilon_{\text{mag}}$	$-\frac{2\epsilon_{\text{mag}}\Lambda^2}{\Lambda^2+(1-\Lambda^2)\sin^2\Phi}$

^a $\Lambda < 1$ is required.

^b Precession phase. $F(\varphi|q)$ and $F(\varphi|1/q)$ are elliptic functions (e.g. Abramowitz & Stegun 1972,)

^c Precession phase per precession cycle.

^d Spin phase per precession cycle.

where $dt/d\phi = 1/\Omega$ and $I_i \simeq I$ in this approximation. The solution to Eq. (55) is a continuous function $t(\phi)$ that exhibits the timing residuals due to spindown; for a single beam, which is appropriate for a precessing pulsar, we evaluate at $\{\phi_i\}$, the discrete set of spin phases where the pulses are beamed toward the observer optimally.

The dependence on precession phase arises from

$$[\hat{\boldsymbol{\mu}} \cdot \hat{\boldsymbol{\ell}}(\Phi)]^2 = \sum_i \hat{\mu}_i^2 \hat{\ell}_i^2 + 2 \sum_{i \neq j} \hat{\mu}_i \hat{\mu}_j \hat{\ell}_i \hat{\ell}_j = \hat{\mu}_1^2 \Lambda^2 + \hat{\mu}_3^2 (1 - \Lambda^2) + \hat{\ell}_2^2 \left(-\frac{\hat{\mu}_1^2 + \hat{\mu}_3^2 e^2}{1 + e^2} + \hat{\mu}_2^2 \right) + 2 \sum_{i \neq j} \hat{\mu}_i \hat{\mu}_j \hat{\ell}_i \hat{\ell}_j, \quad (56)$$

where we used the conservation laws, Eqs. (36) and (40), to separate out the constant term and isolate the dependence on $\hat{\ell}_2^2 \propto \text{sn}^2\Phi$. In evaluating $t(\phi)$ we must be careful to isolate secularly growing terms from terms that are periodic over a precession cycle. We write the solution to Eq. (55) succinctly as

$$t(\phi) = t(0) + \frac{\phi}{\Omega(0)} \left[1 - \frac{2ak\mu^2\Omega(0)}{Ic^3(d\Phi/d\phi)} \sum_{i < j} \hat{\mu}_i \hat{\mu}_j C_{ij} \right] + \frac{k\mu^2\phi^2}{2Ic^3} \left\{ 1 - a \left[\hat{\mu}_1^2 \Lambda^2 + \hat{\mu}_3^2 (1 - \Lambda^2) + \langle \hat{\ell}_2^2 \rangle \left(-\frac{\hat{\mu}_1^2 + \hat{\mu}_3^2 e^2}{1 + e^2} + \hat{\mu}_2^2 \right) \right] \right\} - \frac{ak\mu^2}{Ic^3(d\Phi/d\phi)^2} \left[\left(\hat{\mu}_2^2 - \frac{\hat{\mu}_1^2 + \hat{\mu}_3^2 e^2}{1 + e^2} \right) P_{22}(\Phi) + 2 \sum_{ij} \hat{\mu}_i \hat{\mu}_j P_{ij}(\Phi) \right]. \quad (57)$$

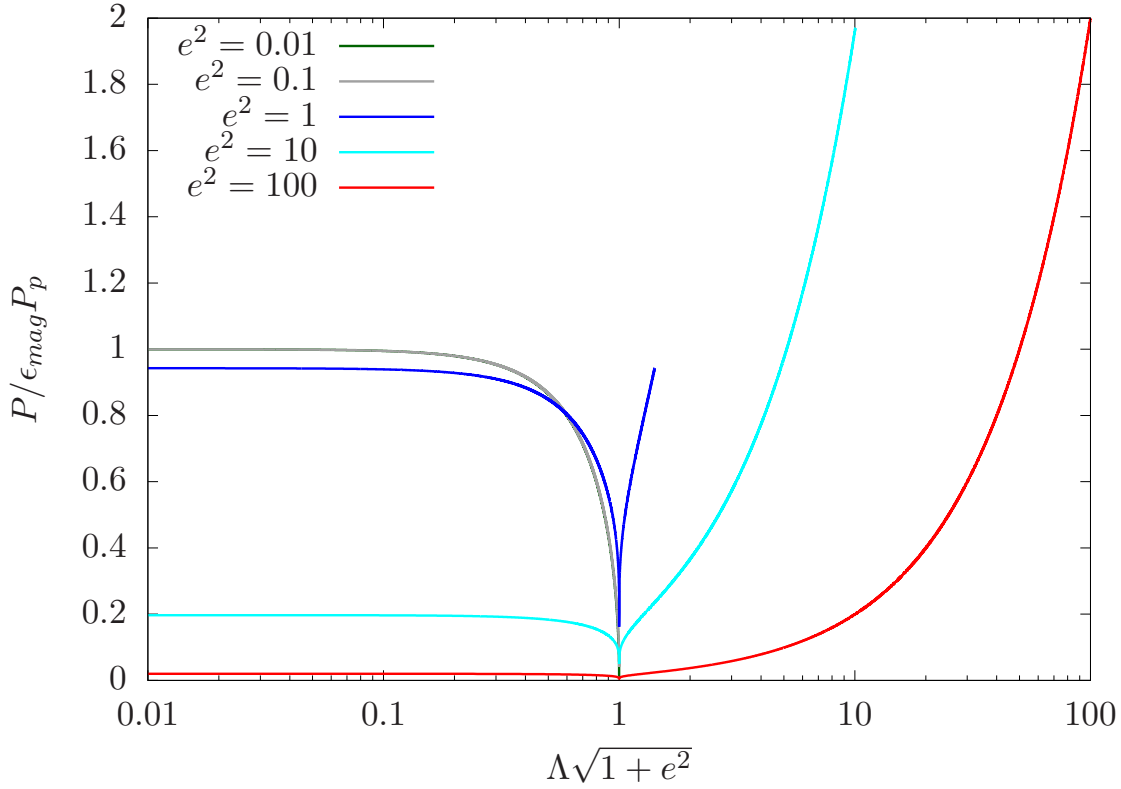


Figure 1. $P/\epsilon_{\text{mag}}P_p$ as a function of $\Lambda\sqrt{1+e^2}$ for $e^2 = 0.01, 0.1, 1, 10$ and 100 .

where $1/\Omega(0) = (dt/d\phi)_0$. Coefficients in Eq. (57) are given in Table 2. The various averages and functions in Table 2 are evaluated in Appendix A.

For calculations, it is convenient to express $t-t(0)$ in terms of the precession period P_p . Then $\phi/\Omega(0)P_p = \Phi/\Phi_{p,\text{cycle}}$ and the remaining terms all depend on the single nondimensional parameter

$$\epsilon_{\text{sd}} = \frac{\mu^2\Omega^2(0)P_p}{I_0c^3} = \frac{P_p}{t_{\text{sd}}} \simeq \frac{2.3 \times 10^{-4} B_{D,14}^2 R_{10}^4 (P_p/100 \text{ d})}{[P(\text{s})]^2 M_{1.4} (I_0/0.2MR^2)} \quad (58)$$

because Eq. (55) may be written in the form

$$\frac{d^2(t/P_p)}{d\Phi^2} = \frac{k\epsilon_{\text{sd}}[1 - a(\hat{\boldsymbol{\mu}} \cdot \hat{\boldsymbol{\ell}})^2]}{\Phi_{p,\text{cycle}}^2}.$$

From Eq. (57) we see that in addition to the apparent frequency shift $\mathcal{O}(\epsilon_{\text{mag}})$ arising from precession there is another apparent frequency shift $\mathcal{O}(\epsilon_{\text{sd}})$. The amplitude of the cyclical terms is of order

$$\Delta t_{\text{sd,cyc}} = \epsilon_{\text{sd}} P_p = \frac{P_p^2}{t_{\text{sd}}} \quad (59)$$

and the cyclical shift in pulse phase due to spindown is of order

$$\Omega(0)\Delta t_{\text{sd,cyc}} = \frac{2\pi\epsilon_{\text{sd}}P_p}{P} = \frac{2\pi P_p^2}{Pt_{\text{sd}}} \quad (60)$$

which can be large for

$$\epsilon_{\text{sd}} \gtrsim \epsilon_{\text{sd},1} \equiv \frac{P}{P_p} \sim \epsilon_{\text{mag}} \quad (61)$$

Table 2. Coefficients in Timing Model

	$q < 1$	$q > 1$
$\langle \hat{\ell}_2^2 \rangle$	$\Lambda^2(1+e^2)\langle \text{sn}^2\Phi \rangle$	$(1-\Lambda^2)(1+1/e^2)\langle \text{sn}^2\Phi \rangle$
C_{12}	$\frac{\Lambda^2\sqrt{1+e^2}(1-\langle \text{dn}\Phi \rangle)}{q^2}$	$\Lambda\sqrt{(1-\Lambda^2)(1+1/e^2)}$
C_{13}	0	0
C_{23}	$\Lambda\sqrt{(1-\Lambda^2)(1+e^2)}$	$q^2(1-\Lambda^2)\sqrt{1+1/e^2}(1-\langle \text{dn}\Phi \rangle)$
P_{12}	$\Lambda^2\sqrt{1+e^2}C_2(\Phi q)$	$-\Lambda\sqrt{(1-\Lambda^2)(1+1/e^2)}C_4(\Phi 1/q)$
P_{13}	$\Lambda\sqrt{1-\Lambda^2}C_3(\Phi q)$	$\Lambda\sqrt{1-\Lambda^2}C_3(\Phi 1/q)$
P_{23}	$-\Lambda\sqrt{(1-\Lambda^2)(1+e^2)}C_4(\Phi q)$	$(1-\Lambda^2)\sqrt{1+1/e^2}C_2(\Phi 1/q)$
P_{22}	$\Lambda^2(1+e^2)C_1(\Phi q)$	$(1-\Lambda^2)(1+1/e^2)C_1(\Phi 1/q)$

(Cordes 1993). The secular terms $\propto \Phi^2$ also become progressively more important for $\epsilon_{\text{sd}} > \epsilon_{\text{sd},1}$ and, if large enough, may frustrate searches for the underlying spin period of the precessing magnetar in models based on stochastic outbursts. Eqs. (58) and (61) imply that

$$\frac{\epsilon_{\text{sd}}}{\epsilon_{\text{sd},1}} = \frac{\mu^2\Omega^2(0)P_p^2}{I_0c^3P} = \frac{1.9 \times 10^3 B_{D,14}^2 R_{10}^4 (P_p/100 \text{ d})^2}{[P(\text{s})]^3 M_{1.4} (I_0/0.2MR^2)} \quad (62)$$

which is between $\sim 5B_{D,14}^2$ and $\sim 5000B_{D,14}^2$ if $P_p = 160 \text{ d}$ (FRB 121102) and between $\sim 0.05B_{D,14}^2$ and $\sim 50B_{D,14}^2$ if $P_p = 16.4 \text{ d}$ (FRB 180916.J0158+65) for $1/P \sim 0.1 - 1 \text{ s}^{-1}$.

2.5. Secular Evolution of Precession via \mathbf{N}_\perp

We now consider how precession evolves as a consequence of spindown, generalizing Goldreich (1970) to cases with $e^2 \neq 0$. As in Goldreich (1970) we consider effects to lowest order in ϵ_{mag} . We generalize the solutions to the Euler equations to include slow evolution of the amplitude parameter $\Lambda = \Lambda(\epsilon t)$, as was done by Goldreich (1970), but also include a slowly varying phase shift by replacing $\Phi = (d\Phi/d\phi)\phi$ with $\tilde{\Phi}(t) = \Phi + \psi(\epsilon t)$. This phase shift is required for triaxial precession evolving via spindown. Here $\epsilon = ak\mu^2(L/I_3)^2/c^3I_3$ is roughly the inverse spindown time. We assume that the spindown time is long compared with the precession timescale, a necessary condition for a perturbative treatment; this assumption fails at early times, or if $\Lambda\sqrt{1+e^2} \rightarrow 1$.

We start by considering $\Lambda\sqrt{1+e^2} < 1$, which is favored for long precession periods, and is the expected state if precession is excited from rotation about \hat{e}_3 with relatively low δE_p . Averaging over precession phase we find

$$\begin{aligned} \frac{1}{q} \frac{dq}{dt} &= \frac{ak\mu^2(L/I_3)^2}{c^3I_3} \{ \hat{\mu}_1^2 [2 - (1+q^2)\langle \text{sn}^2\Phi \rangle] + \hat{\mu}_2^2 [1 + (1-2q^2)\langle \text{sn}^2\Phi \rangle] - (1-q^2\langle \text{sn}^2\Phi \rangle) \} \\ \frac{d\psi}{dt} &= \frac{ak\mu^2(L/I_3)^2 \hat{\mu}_1 \hat{\mu}_2}{c^3I_3\sqrt{1+e^2}} \left[\left\langle \frac{\text{cn}^2\Phi}{\text{dn}\Phi} \right\rangle - (1+e^2) \left\langle \frac{\text{sn}^2\Phi}{\text{dn}\Phi} \right\rangle \right]. \end{aligned} \quad (63)$$

where we used

$$\frac{dq}{q} = \frac{d\Lambda}{\Lambda} - \frac{d\sqrt{1-\Lambda^2}}{\sqrt{1-\Lambda^2}} = \frac{d\Lambda}{\Lambda} + \frac{\Lambda d\Lambda}{1-\Lambda^2} = \frac{d\Lambda}{\Lambda(1-\Lambda^2)} - \frac{d\sqrt{1-\Lambda^2}}{\Lambda^2\sqrt{1-\Lambda^2}}. \quad (64)$$

Eq. (63) reduces to the results in Goldreich (1970) for $e^2 = 0$, the axisymmetric oblate case, for which $\langle \text{cn}^2\Phi \rangle = \langle \text{sn}^2\Phi \rangle = \frac{1}{2}$ and $\text{dn}\Phi = 1$, after replacing $dq/q \rightarrow d\Lambda/\Lambda(1-\Lambda^2)$ using Eq. (64); for that case, there is no phase shift ψ . The stability condition implied by the first of Eqs. (63) is more complicated than what was found by Goldreich (1970) for the axisymmetric, oblate case: there is a separatrix that is an ellipse in the $\hat{\mu}_1 - \hat{\mu}_2$ plane whose axes depend on q , so that, for given values of e^2 and $\hat{\mu}_1^2$ and $\hat{\mu}_2^2$, there is a fixed point at a specific value of q .

By contrast, for the axisymmetric oblate case, the ellipse degenerates into a circle

$$\hat{\mu}_1^2 + \hat{\mu}_2^2 = \frac{2}{3} \quad (65)$$

irrespective of the value of Λ . In this case, Λ grows as long as the magnetic moment configuration of the star is outside this circle. The growth halts once $\Lambda \rightarrow 1$, where $d\Lambda/dt$ also goes to zero. Inside the circle, Λ decreases, reaching $\Lambda = 0$ asymptotically.

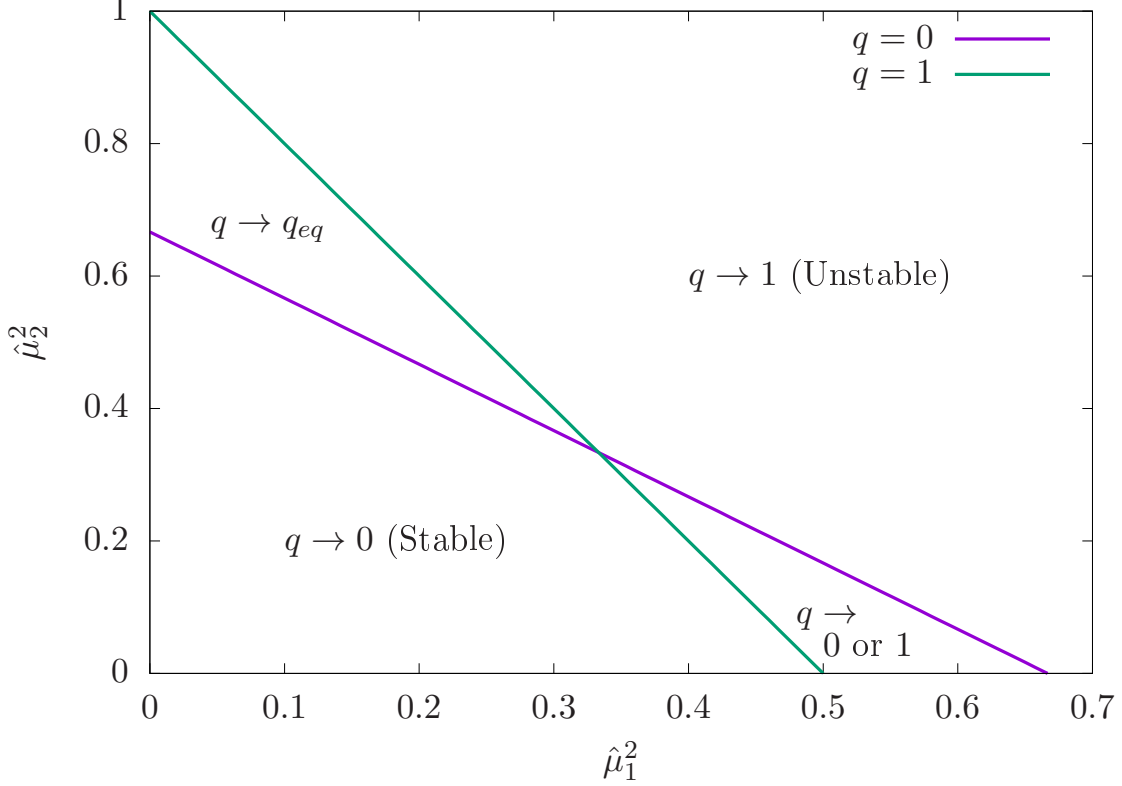


Figure 2. Stability boundaries for $q = 0$ and $q = 1$ and outcomes for secular evolution of q .

For the triaxial case q cannot grow beyond $q = 1$; since $\langle \text{sn}^2\Phi \rangle = 1$ for $q = 1$, Eq. (63) implies $dq/dt = 0$. The stability curve (infinitesimally) close to $q^2 = 1$ is

$$2\hat{\mu}_1^2 + \hat{\mu}_2^2 = 1. \quad (66)$$

The two curves intersect at $\hat{\mu}_1^2 = \hat{\mu}_2^2 = 1/3$; in fact all of the stability boundaries intersect at this point since $\langle \text{cn}^2\Phi \rangle = 1 - \langle \text{sn}^2\Phi \rangle$ and $\langle \text{dn}^2\Phi \rangle = 1 - q^2\langle \text{sn}^2\Phi \rangle$. These two bounding stability lines are depicted in Fig. 2. The stability boundaries for all other values of q are between these two lines, pivoting about their intersection point at $\hat{\mu}_1^2 = \hat{\mu}_2^2 = 1/3$.

Fig. 2 depicts evolution outcomes for various regions in the $\mu_1^2 - \mu_2^2$ phase plane. The region marked “ $q \rightarrow 1$ ” is unconditionally unstable: if precession is excited for (μ_1^2, μ_2^2) in this region, q grows on the spindown timescale until $q = 1$, where growth ceases. Conversely, the region marked “ $q \rightarrow 0$ ” is unconditionally stable: if precession is excited for (μ_1^2, μ_2^2) in this region, q shrinks toward zero on the spindown timescale. In the two triangular regions between the $q = 0$ and $q = 1$ bounding curves $dq/dt = 0$ at $q = q_{\text{eq}}(\mu_1^2, \mu_2^2)$ for each (μ_1^2, μ_2^2) . In the region marked “ $q \rightarrow q_{\text{eq}}$,” $dq/dt < 0$ for $q > q_{\text{eq}}(\mu_1^2, \mu_2^2)$ and $dq/dt > 0$ for $q < q_{\text{eq}}(\mu_1^2, \mu_2^2)$, so if precession is excited in this region $q \rightarrow q_{\text{eq}}(\mu_1^2, \mu_2^2)$ asymptotically as a result of spindown. In the region marked “ $q \rightarrow 0$ or 1”, $dq/dt > 0$ for $q > q_{\text{eq}}(\mu_1^2, \mu_2^2)$ so $q \rightarrow 1$ asymptotically if precession is excited with $q > q_{\text{eq}}(\mu_1^2, \mu_2^2)$ and $dq/dt < 0$ for $q < q_{\text{eq}}(\mu_1^2, \mu_2^2)$ so $q \rightarrow 0$ asymptotically if precession is excited with $q < q_{\text{eq}}(\mu_1^2, \mu_2^2)$.

For precession in the $\Lambda\sqrt{1+e^2} > 1$ regime we get

$$\begin{aligned} -\frac{1}{q} \frac{dq}{dt} &= \frac{ak\mu^2(L/I_3)^2}{c^3 I_3} \left\{ \hat{\mu}_3^2 \left[2 - \left(1 + \frac{1}{q^2} \right) \langle \text{sn}^2\Phi \rangle \right] + \hat{\mu}_2^2 \left[1 + \left(1 - \frac{2}{q^2} \right) \langle \text{sn}^2\Phi \rangle \right] - \left(1 - \frac{\langle \text{sn}^2\Phi \rangle}{q^2} \right) \right\} \\ \frac{d\psi}{dt} &= \frac{ak\mu^2(L/I_3)^2 \hat{\mu}_3 \hat{\mu}_2 e}{c^3 I_3 \sqrt{1+e^2}} \left[\left\langle \frac{\text{cn}^2\Phi}{\text{dn}\Phi} \right\rangle - \left(1 + \frac{1}{e^2} \right) \left\langle \frac{\text{sn}^2\Phi}{\text{dn}\Phi} \right\rangle \right], \end{aligned} \quad (67)$$

where we used Eq. (64) again. Eq. (67) may be obtained from Eq. (63) with the substitutions $\hat{\mu}_1^2 \rightarrow \hat{\mu}_3^2$, $e^2 \rightarrow 1/e^2$ and $q \rightarrow 1/q$. The evolution scenarios for $1/q$ analogous to those for q shown in Fig. 2 may be derived using this mapping.

3. APPLICATION TO FAST RADIO BURSTS

3.1. A Random Burst Model

To this point, we have focussed on the combined effects of precession and spindown on observations of emission along a single beam in which emitted intensity is determined entirely by $\hat{\mathbf{b}} \cdot \hat{\mathbf{n}}$. For application to FRBs we develop a different model in which multiple beams pointing in random directions fire at random times with random intrinsic intensities.

To address these questions we simulate an ideal observing program consisting of daily observations over a total observing time lasting $n_{\text{p,cycle}}$ precession cycles. In our idealized observing campaign, each daily observation starts one day after the beginning of the previous one and lasts f_{obs} days (2.4 hours). We assume that bursts occur at a uniform rate throughout the duration of the observing program and that n_{bursts} occur during the total time $f_{\text{obs}} n_{\text{p,cycle}} P_p$ of the observations. We input P_p in days, so that the number of observing days is the integer part of P_p plus one.

We also input the parameters of the precession model, $(\epsilon_{\text{mag}}, \Lambda, e^2)$ from which we can compute the spin frequency ν_* . We choose $\gamma(0)$ randomly in the range $[0, 2\pi]$.

The simulation starts by choosing the set $\{\Phi_j\}$ of individual burst precession phases; in the absence of spindown the corresponding burst times are $t_j = P_p \Phi_j / \Phi_{\text{p,cycle}}$, and even with spindown included the burst times only differ from these times by $\mathcal{O}(\epsilon_{\text{sd}})$. For each simulation there are n_{bursts} bursts. Ultimately, only a small fraction of these are detectable.

For each Φ_j we next determine a beam direction $\hat{\mathbf{b}}_j$ in the rotating frame of reference. We do this relative to a reference beam whose direction we input. In the calculations presented here we assume that this reference direction coincides with the direction of the dipole moment appearing in the spindown formula, $\hat{\boldsymbol{\mu}}$. We assume that $\hat{\mathbf{b}}_j$ is anywhere between two cones about $\hat{\boldsymbol{\mu}}$ defined by $\cos \theta_{\text{min}} \leq \hat{\mathbf{b}}_j \cdot \hat{\boldsymbol{\mu}} \leq \cos \theta_{\text{max}}$, adopting a uniform distribution for $\hat{\mathbf{b}}_j \cdot \hat{\boldsymbol{\mu}}$ over this range and a uniform direction of azimuthal angles in $[0, 2\pi]$. We could, of course, choose a different reference direction or multiple reference directions among which bursts may switch. As should already be apparent, there are many parameters in this model, and choosing a single reference direction simplifies the calculation somewhat. Our model does allow the reference direction to switch to a different one with a probability $p_{\text{flip}} = 1 - f_{\text{no flip}}$, but the results reported here are for $p_{\text{flip}} = 0$.

The next step is to compute $\hat{\mathbf{b}}_j \cdot \hat{\mathbf{n}}$ for each outburst. We do this by computing $\hat{\mathbf{n}}(\Phi_j)$ in the rotating frame of reference from Eq. (52). This requires choosing a value of the inclination angle i defined in Eq. (48), which we input.

Once we have the value of $\hat{\mathbf{b}}_j \cdot \hat{\mathbf{n}}(\Phi_j) \equiv \hat{\mathbf{b}}_j \cdot \hat{\mathbf{n}}_j$ for a given outburst we can decide whether or not that outburst is detectable. As a first cut, we discard all bursts for which $\hat{\mathbf{b}}_j \cdot \hat{\mathbf{n}}_j < 0$ since these point away from the observer. Because we assume that each beam has a FWHM θ_{FWHM} we may be discarding some bursts that could be detectable, in principle, but as long as θ_{FWHM} is not too large we expect that this is not an important source of inaccuracy in our conclusions. We do not discard beams that would be eclipsed by the neutron star. To do that we would need to specify the radius r_b from which emission originates for beam b ; eclipses could occur for $\cos \theta_b < 0$ and $\pi - \theta_b \lesssim R/r_b$. In most of our simulations we restrict $\cos \theta_b \geq 0$.

We assume a Gaussian emission pattern for each beam with an intrinsic intensity

$$I_j(\hat{\mathbf{b}} \cdot \hat{\mathbf{n}}) = I_j(1) \exp[\kappa(\hat{\mathbf{b}}_j \cdot \hat{\mathbf{n}}_j - 1)] \quad (68)$$

where, if the FWHM of the beam is θ_{FWHM} ,

$$\kappa = \frac{\ln 2}{1 - \cos(\frac{1}{2}\theta_{\text{FWHM}})} ; \quad (69)$$

$I_j(1)$ is the peak intensity for outburst j and

$$\int_0^1 d\mu I_j(\mu) = \frac{2\pi I_j(1)[1 - \exp(-\kappa)]}{\kappa} \quad (70)$$

is the total intensity of the beam integrated over directions. Eq. (68) would be the final answer if all outbursts were equally intense intrinsically, but in general we expect a distribution of $I_j(1)$. To model this, we input a range

of intrinsic intensities, and assume that the distribution of intrinsic intensities $I_j(1)$ is uniform in $\ln I_j(1)$ over the corresponding logarithmic range with a mean value of one. (In this model we could choose a different mean value, but this would just introduce a multiplicative factor in each value of $I_j(1)$.) After selecting $\ln I_j(1)$ at random from this distribution we evaluate I_j using Eq. (68).

Given $\{I_j\}$ we can find the maximum value I_{\max} . We assume that only bursts greater than $I_{\min} = I_{\max} \times (I_{\min}/I_{\max})$ are detectable, where I_{\min}/I_{\max} is another input parameter. We then have the sets $\{\Phi_j\}$ and $\{I_j/I_{\max}\}$ for the bursts. The latter can immediately be turned into a plot of number of detected bursts per (daily) observing session versus precession phase, which provides a simple visual indication of whether the data reveal or conceal the precession period. The same data can be plotted as a cumulative distribution of observed burst intensities which we shall see is different from the inputted distribution of intrinsic burst intensities.

The final step in our calculations is to determine conditions under which the spin frequency ought to be detected. We do this by computing

$$\hat{D}(\nu_\star) = \sum_j w_j \exp[2\pi i \nu_\star t(\Phi_j)] \quad (71)$$

where $\nu_\star = \Omega(0)/2\pi$ is the (initial) spin frequency of the star and $t(\Phi_j)$ is computed from Eq. (57) for selected values of ϵ_{sd} . In Eq. (71) $\{w_j\}$ is a set of weights assigned to each detected burst. To assess the evidence for a given ν we compute $|D(\nu)|$. For totally uncorrelated t_j

$$\langle |\hat{D}(\nu_\star)|^2 \rangle_{\text{uncorrelated}} = \sum_j w_j^2 \quad (72)$$

so we normalize the computed values:

$$|\hat{D}(\nu_\star)|_{\text{normalized}} \equiv \frac{|\hat{D}(\nu_\star)|}{\sqrt{\langle |\hat{D}(\nu_\star)|^2 \rangle_{\text{uncorrelated}}}} \quad (73)$$

In our calculations we weight each term in Eq. (71) equally, so that $w_j = 1/N_{\text{bursts}}$ for N_{bursts} detected bursts; with this choice $\langle |D(\nu)|^2 \rangle_{\text{uncorrelated}} = 1/N_{\text{bursts}}$, and

$$|\hat{D}(\nu_\star)|_{\text{normalized}} \equiv |\hat{D}(\nu_\star)| \sqrt{N_{\text{bursts}}} \quad (74)$$

Another plausible choice for w_j would be I_j/I_{\max} . If the burst times are precisely periodic then $|\hat{D}(\nu_\star)| = 1$ and $|\hat{D}(\nu_\star)|_{\text{normalized}} = \sqrt{N_{\text{bursts}}}$. This remains true for $\nu'_\star = \nu_\star + \Delta\nu_\star$; the frequency shift associated with spindown, which is included in our calculation, is undetectable. For a single beam, there would be a systematic frequency shift $\mathcal{O}(\epsilon_{\text{mag}})$ that depends on beam direction, but for multiple beams there is no systematic shift. The value of $|\hat{D}(\nu_\star)|$ is unaffected by shifting the burst times by a common time offset. If burst times are random, the asymptotic probability distribution of $r = |\hat{D}(\nu_\star)| \sqrt{N}$ is

$$\frac{dp(r)}{dr} = 2r \exp(-r^2) \quad (75)$$

independent of N . The mode of Eq. (75) is $r = 1/\sqrt{2}$ and the mean is $\sqrt{\pi}/2$.

In our models, we evaluate $D_d(\nu_\star) = |\hat{D}(\nu_\star)| \sqrt{N_d}$ for each of $\{d\}$ days of observations during which $\{N_d\}$ bursts are detected. According to Eq. (75) the probability that $D_d > r$ is $\exp(-r^2)$ if the bursts occur randomly. If observations are done on M days the expected number of values of D_d that exceed r is $n(> r) = M \exp(-r^2)$, and the value of r for which $(n > r) = 1$ is

$$r_1(M) = \sqrt{\ln M} \quad (76)$$

The probability that no values of $|\hat{D}_d(\nu_\star)| \sqrt{N_d} > r_0$ are found at random is

$$p(r_0, M) = [1 - \exp(-r_0^2)]^M$$

so for a chosen value $p = p(r_0|M)$

$$r_0(p, M) = \frac{1}{\sqrt{\ln(1 - p^{1/M})}} = \frac{1}{\sqrt{\ln[1 - \exp(\ln p)/M]}} \approx \frac{1}{\sqrt{-\ln p/M}} = \frac{r_1(M)}{\sqrt{-\ln p}}; \quad (77)$$

$r_1(M) \approx r_0(1/e, M)$. Below we use $r_1(M)$ to assess the detectability of ν_* over M days by keeping track of the number of days for which $\hat{D}_d(\nu_*)$ exceeds $r_1(M)$.

Of course the observer will not know ν_* in advance but we presume that he/she analyzes the data for a broad range of possible spin frequencies including test values near ν_* . In our simulations, we compute $\{\hat{D}_d(\nu_*)\}$ for each of $M = 512$ consecutive days, so $r_1(M) = \sqrt{\ln 512} = 2.498$. We focus on the day with the largest value $\hat{D}_d(\nu_*)\sqrt{N_d}$ and for that day we calculate $\hat{D}_d(\nu)\sqrt{N_d}$ for N_{freq} different frequencies. For small enough spacing between the test frequencies ν_* ought to be very near one of the sampled frequencies; a value above $r_1(N_{\text{freq}})$ is considered to be significant. In the simulations reported in Table 3 we sample frequencies spaced by $\Delta\nu/\nu = 10^{-5}$ Hz between 0.05 Hz and 5 Hz, a total of $N_{\text{freq}} = 460518$ frequencies, so $r_1(N_{\text{freq}}) = \sqrt{\ln 460518} = 3.611$. Although we have only done frequency searches on the most promising day for each burst model, the spin frequency ought to be detectable on any day for which $\hat{D}_d(\nu_*)\sqrt{N_d} > r_1(N_{\text{freq}})$, so we tabulate the number of such days.

In Appendix B we develop an analytic theory of the probability of burst detections at a given time in our model. Eq. (B1) makes it clear that the probability depends on spin and precession frequency via $\hat{\mathbf{n}}(\Phi) \cdot \hat{\boldsymbol{\mu}}$. Moreover, there is no time dependence at all if the distribution of beam directions is isotropic. Thus, the observation of regular precession cycles by itself argues for a restricted range of beam directions.

Table 3. Simulated Burst Models^a

P_p (d)	ϵ_{mag}	Λ	ν_* (Hz)	$\cos \theta_b$ ^b	D_{max} (d) ^c	N_{bursts} (%) ^d	$N_d(512)$ ^e	$N_d(N_{\text{freq}})$ ^f	Description
160	10^{-6}	0.2	0.1521	[0.99,1]	13.6 (411)	37596 (3.7%)	399	384	pulsar-like
160	10^{-7}	0.2	1.521	[0.99,1]	13.0 (414)	37017 (3.6%)	403	386	pulsar-like
16.4	10^{-5}	0.2	0.1484	[0.99,1]	13.0 (48)	40280 (3.9%)	417	403	pulsar-like
16.4	10^{-6}	0.2	1.484	[0.99,1]	12.8 (109)	39497 (3.9%)	416	403	pulsar-like
160	10^{-6}	0.2	0.1521	[0,1]	4.46 (443)	29864 (2.9%)	114	13	hemisphere
160	10^{-7}	0.2	1.521	[0,1]	4.40 (427)	29663 (2.9%)	114	11	hemisphere
16.4	10^{-5}	0.2	0.1484	[0,1]	4.24 (341)	29333 (2.9%)	110	8	hemisphere
16.4	10^{-6}	0.2	1.484	[0,1]	4.05 (488)	29456 (2.9%)	109	12	hemisphere
160	10^{-6}	0.2	0.1521	[0.1,0.8]	3.22 (438)	28965 (2.8%)	17	0	inter-cone
160	10^{-7}	0.2	1.521	[0.1,0.8]	3.79 (377)	29030 (2.8%)	24	2	inter-cone
16.4	10^{-5}	0.2	0.1484	[0.1,0.8]	2.90 (37)	28630 (2.8%)	8	0	inter-cone
16.4	10^{-6}	0.2	1.484	[0.1,0.8]	3.36 (168)	28290 (2.8%)	13	0	inter-cone
160	10^{-6}	0.44	0.1071	[0.99,1]	13.1 (352)	16682 (1.6%)	181	164	pulsar-like
160	10^{-7}	0.44	1.071	[0.99,1]	12.6 (32)	16541 (1.6%)	182	169	pulsar-like
16.4	10^{-5}	0.44	0.1045	[0.99,1]	12.9 (86)	16747 (1.6%)	181	168	pulsar-like
16.4	10^{-6}	0.44	1.045	[0.99,1]	12.9 (431)	16784 (1.6%)	179	166	pulsar-like
160	10^{-6}	0.44	0.1071	[0,1]	5.07 (50)	21334 (2.1%)	326	157	hemisphere
160	10^{-7}	0.44	1.071	[0,1]	4.85 (445)	21158 (2.1%)	317	143	hemisphere
16.4	10^{-5}	0.44	0.1045	[0,1]	4.80 (418)	20322 (2.0%)	336	149	hemisphere
16.4	10^{-6}	0.44	1.045	[0,1]	5.20 (187)	20799 (2.0%)	343	177	hemisphere
160	10^{-6}	0.44	0.1071	[0.1,0.8]	5.61 (390)	22160 (2.2%)	271	179	inter-cone
160	10^{-7}	0.44	1.071	[0.1,0.8]	5.65 (433)	22335 (2.2%)	278	177	inter-cone
16.4	10^{-5}	0.44	0.1045	[0.1,0.8]	5.46 (46)	21615 (2.1%)	299	185	inter-cone
16.4	10^{-6}	0.44	1.045	[0.1,0.8]	5.37 (385)	21268 (2.1%)	300	193	inter-cone

^a Consecutive daily observations lasting 0.1 d each for 512 d, observer at $i = 52^\circ$. A total of 1024000 outbursts. Beam width $\theta_{\text{FWHM}} = 20^\circ$. Intrinsic intensity range a factor of 1000; ratio of minimum to maximum observed intensities $I_{\text{min}}/I_{\text{max}} = 0.01$. $\epsilon_{\text{sd}} = 0$.

^b Range of beam offsets axisymmetric relative to symmetry axis at $\hat{\mathbf{e}}_3 \cos \theta_\mu + \sin \theta_\mu (\hat{\mathbf{e}}_1 \cos \varphi_\mu + \hat{\mathbf{e}}_2 \sin \varphi_\mu)$ with $(\theta_\mu, \varphi_\mu) = (30^\circ, 40^\circ)$.

^c Maximum value of $\hat{D}_d\sqrt{N_d}$ and day on which it occurs.

^d Total number of detectable bursts and fraction of total number of outbursts.

^e Number of days for which $\hat{D}_d\sqrt{N_d}$ exceeds $\sqrt{\ln 512} = 2.498 \dots$

^f Number of days for which $\hat{D}_d\sqrt{N_d}$ exceeds $\sqrt{\ln N_{\text{freq}}} = 3.611 \dots$

3.2. Results

Given the large number of parameters, we have not done a systematic, complete exploration of the multidimensional phase space of models. However, we have explored numerous particular cases to look for trends related to the two phenomenological questions above. In doing this, we held one parameter not listed in Table 3 fixed for most runs: the initial value of the random number seed. Normally, this is Monte Carlo malpractice. Two models with identical initial random number seed and the same value of n_{bursts} and same ranges of $\cos \theta_b$ and $I_j(1)$ will start with identical sets of outbursts; that is $\{\Phi_j, \hat{\mathbf{b}}_j, I_j(1)\}$ will be the same. However, two models with the same e^2 but different values of Λ will have different $\{\hat{\mathbf{n}}_j\}$ hence different $\{\hat{\mathbf{b}}_j \cdot \hat{\mathbf{n}}_j\}$ and different intensities $\{I_j\}$ so their subsets of detectable outbursts will be different. Models with different ranges of $\cos \theta_b$ and $I_j(1)$ start with identical sets of $\{\Phi_j\}$ which isolates the differences in properties of detectable bursts associated with emitting geometry and precession. Here and there we verified that the initial random number seed was not critical to qualitative features of the results.

For n_{bursts} in a total observing time $t_{\text{obs}} = f_d n_{\text{p,cycle}} P_p$, the burst rate is $n_{\text{bursts}}/t_{\text{obs}}$; for the simulations listed in Table 3 $t_{\text{obs}} = 51.2$ d and the burst rate is $1024000/51.2 \text{ d} = 20,000 \text{ d}^{-1} = 0.231 \text{ Hz}$. For our simulations, $\nu_* \simeq 0.1, 0.15, 1$ or 1.5 Hz so the number of outbursts per spin period ranges from $\simeq 0.15$ to $\simeq 2.3$. If all of these bursts were detectable, the spin frequency of the magnetar would be easy to find. In the simulation results, the burst detection efficiency is *at most* $\simeq 4\%$, which would correspond to *at most* of order one burst per ten spin periods which, although not large, should still suffice to uncover the underlying spin period. The total number of outbursts was chosen so that the average number of *detected* bursts per day would turn out to be ~ 50 in the simulations. This detection rate is comparable to the rate reported by Li et al. (2021) for about 50 days of observations of FRB 121102. No convincing evidence for a spin frequency was found by Li et al. (2021).

Table 3 tabulates results for sixteen simulations. For all of these

1. $e^2 = 10$,
2. the distribution of intrinsic intensities ranges over a factor of 1000,
3. the beam width is $\theta_{\text{FWHM}} = 20^\circ$,
4. bursts are detectable over a range of observed intensities $I_{\text{max}}/I_{\text{min}} = 1000$,
5. the distribution of beam directions is axisymmetric about symmetry axis $\hat{\boldsymbol{\mu}} = \hat{\mathbf{e}}_3 \cos \theta_\mu + \sin \theta_\mu (\hat{\mathbf{e}}_1 \cos \varphi_\mu + \hat{\mathbf{e}}_2 \sin \varphi_\mu)$ with $(\theta_\mu, \varphi_\mu) = (30^\circ, 40^\circ)$,
6. there are daily observations lasting 0.1 d each over a total timespan of 512 d,
7. and the observer is at $i = 52^\circ$ relative to the spin angular momentum of the star (Eq. (48)).

The average number of bursts per day is $\sim 30 - 60$ for all of the tabulated models. Although the tabulated models are for $\epsilon_{\text{sd}} = 0$ we do not regard this as an essential limitation for two reasons. First, as omniscient simulators, we can nullify the effects of spindown entirely by adjusting the value of the frequency tested from ν_* to $\nu_{*,\text{d}}$; our code allows us to do this, and we have verified that $\hat{D}_d(\nu_{*,\text{d}})$ with $\epsilon_{\text{sd}} \neq 0$ is virtually the same as $\hat{D}(\nu_*)$ with $\epsilon_{\text{sd}} = 0$. Second, we do frequency searches on the most promising day with $\epsilon_{\text{sd}} \neq 0$ and detect frequency shifts for large enough spindown compared to our frequency resolution.

The table is divided into two categories, $\Lambda = 0.2$ and $\Lambda = 0.44$; more precisely $q^2 = 5/12$ for the upper half of the table and $q^2 = 12/5$ for the lower half. Each half is subdivided into three parts that are distinguished by different ranges of beam directions:

1. “pulsar-like” models only allow beams in a very narrow cone of angles around $\hat{\boldsymbol{\mu}}$, $0.99 \leq \cos \theta_b \leq 1$;
2. “hemisphere” models allow beams in any direction in the outward hemisphere relative to $\hat{\boldsymbol{\mu}}$, $0 \leq \cos \theta_b \leq 1$;
3. “inter-cone” models allow beams between the cones defined by $\cos \theta_{\text{min}} = 0.1$ and $\cos \theta_{\text{max}} = 0.8$ around $\hat{\boldsymbol{\mu}}$.

Inter-cone models exclude beams in a fairly narrow cone near the symmetry axis as well as beams orthogonal to it. A number of trends are apparent in Table 3:

1. more bursts are detectable for $\Lambda = 0.2$ than for $\Lambda = 0.44$ in all cases;

2. for either value of Λ all subcategories – pulsar-like, hemisphere, intercone – give similar results irrespective of the value of ϵ_{mag} ;
3. ν_* is readily detectable on $\sim 30\%$ of days for $\Lambda = 0.44$ for pulsar-like, hemisphere and intercone geometries;
4. ν_* is detectable on $\lesssim 3\%$ of all days for hemisphere models with $\Lambda = 0.2$, but reproducible results for ν_* (modulo spindown) ought to emerge in a dedicated program of nearly daily observations that lasts long enough;
5. ν_* is largely undetectable for inter-cone models with $\Lambda = 0.2$.

The uniformity of results within the various subcategories is not a complete surprise since $160/16.4$ is near ten so models with $P_p = 160$ d and a given value of ϵ_{mag} are ought to resemble models with $P_p = 16.4$ d and $10\epsilon_{\text{mag}}$ closely. The dependence on ϵ_{mag} for a given value of P_p is weak. The detection criteria in our simulations only depend on spin frequency implicitly via $\hat{\mathbf{b}} \cdot \hat{\mathbf{n}}(\Phi)$, but this dependence is weak because $\hat{\mathbf{b}}$ varies widely and stochastically (except in the pulsar-like models). We expect that as long as the time between bursts is large compared with $1/\nu_*$ final results should be insensitive to ϵ_{mag} .

Although we have not tabulated results for models in which beams can point in any direction (i.e. $-1 \leq \cos \theta_b \leq 1$) we have simulated such models; in general neither ν_* nor P_p is apparent in the results.

Fig. 3 shows numerical results for two models where ν_* ought to be detected. All of these results are for $P_p = 160$ d, $\epsilon_{\text{mag}} = 10^{-6}$ and $\Lambda = 0.2$, so that $\nu_* = 0.1521$ Hz. The top panels are for the pulsar-like case and the bottom for the hemisphere case. The left panels in both rows show $N_d/10$ for each day (purple crosses); the precession cycle is evident in both panels. These panels also show $\hat{D}_d(\nu_*)\sqrt{N_d}$ for each day (green x's), with the day on which $\hat{D}_d(\nu_*)\sqrt{N_d}$ is largest indicated by a downward arrow. The horizontal red lines in each figure are at $r_1(N_{\text{freq}}) = \sqrt{\ln N_{\text{freq}}} \simeq 3.611$, which we take to be the threshold for detection of ν_* . The right panels show the results of a period search on the most favorable day for detecting ν_* using $N_{\text{freq}} = 460518$ test frequencies spaced at equal logarithmic intervals $\Delta\nu/\nu \simeq 10^{-5}$ between 0.05 Hz and 5 Hz. The value of $\hat{D}_d(\nu_*)\sqrt{N_d}$ exactly at ν_* is also shown as an orange triangle. The leftmost vertical dashed lines are at the spin frequencies for these two models; for the pulsar-like model vertical dashed lines at four harmonics of ν_* are also shown. The spin frequency and four harmonics are found easily for the pulsar-like model; the spin frequency is also found for the hemisphere model.

Fig. 4 shows numerical results for two inter-cone models with $P_p = 160$ d and $\epsilon_{\text{mag}} = 10^{-7}$ (top) and $\epsilon_{\text{mag}} = 10^{-6}$ (bottom). For $\epsilon_{\text{mag}} = 10^{-7}$ the spin frequency should be detectable, whereas for $\epsilon_{\text{mag}} = 10^{-6}$ it is not. The spin frequency would be found significantly for $\epsilon_{\text{mag}} = 10^{-7}$, but a slightly larger value of $|\hat{D}(\nu)|\sqrt{N_d}$ is found around 1.7 Hz;. This is not particularly troubling since both frequencies have values of $|\hat{D}(\nu)|\sqrt{N_d}$ close to $r_1(N_{\text{freq}})$, but it suggests that ν_* would not be detected on this particular day. (We reran this case with a different random number seed and found that $|\hat{D}(\nu)|\sqrt{N_d} < r_1(N_{\text{freq}})$ on all days.) The spin frequency would not be found for $\epsilon_{\text{mag}} = 10^{-6}$.

So far, we have concentrated on searching for ν_* on individual days, presenting frequency spectra only on the most promising days for detection. Alternatively, the frequency search can be performed on the entire data set. Fig 5 shows results for the cumulative value $|\hat{D}(\nu_*, \leq d)|$ computed by performing the sum Eq. (71) over the $N(\leq d)$ bursts detected up to the end of day d and multiplying by $\sqrt{N(\leq d)}$. All four panels in Fig. 5 are computed for nested-cone geometry with $0.1 \leq \cos \theta_b \leq 0.8$. The top panels are for $P_p = 160$ d and $\epsilon_{\text{mag}} = 10^{-6}$ and the bottom for $P_p = 16.4$ d and $\epsilon_{\text{mag}} = 10^{-5}$ so spin frequencies are comparable in all cases. The left panels are for $\Lambda = 0.2$, where Table 3 indicates no promising days for burst detections, and the right panels are for $\Lambda = 0.44$, for which we expect ≈ 200 promising days. The top left panel shows that the value of $|\hat{D}(\nu_*, \leq d)|\sqrt{N(\leq d)}$ generally increases with d for $\epsilon_{\text{sd}} = 0$, apart from fluctuations, suggesting that detection may be possible in a cumulative analysis. However, Eq. (62) implies that $\epsilon_{\text{sd}}/\epsilon_{\text{sd},1} \approx 17B_{D,14}^2$ for the top left panel in Fig. 5 and $\approx 6B_{D,14}^2$ for the right panel. At these levels, the accumulated spindown over many days of observation becomes important, and discovering ν_* from a cumulative analysis that neglects spindown is problematic. The situation for $P_p = 16.4$ d appears to be more complicated. As the left panel shows, although $|\hat{D}(\nu_*, \leq d)|\sqrt{N(\leq d)}$ increases at first for $\epsilon_{\text{sd}} = 0$, ultimately it decreases while fluctuating considerably; the same sort of behavior is evident in the right panel. For these cases, $\epsilon_{\text{sd}} \approx 0.17B_{D,14}^2\epsilon_{\text{sd},1}$ and $0.06B_{D,14}^2\epsilon_{\text{sd},1}$, respectively, so spindown is less important for $B_{D,14} = 1$. We show what happens for $\epsilon_{\text{sd}} = \epsilon_{\text{sd},1}$ in both panels: spindown this fast further suppresses accumulation of evidence for ν_* in the left panel, but actually can enhance it, at least for awhile, in the case depicted in the right panel.

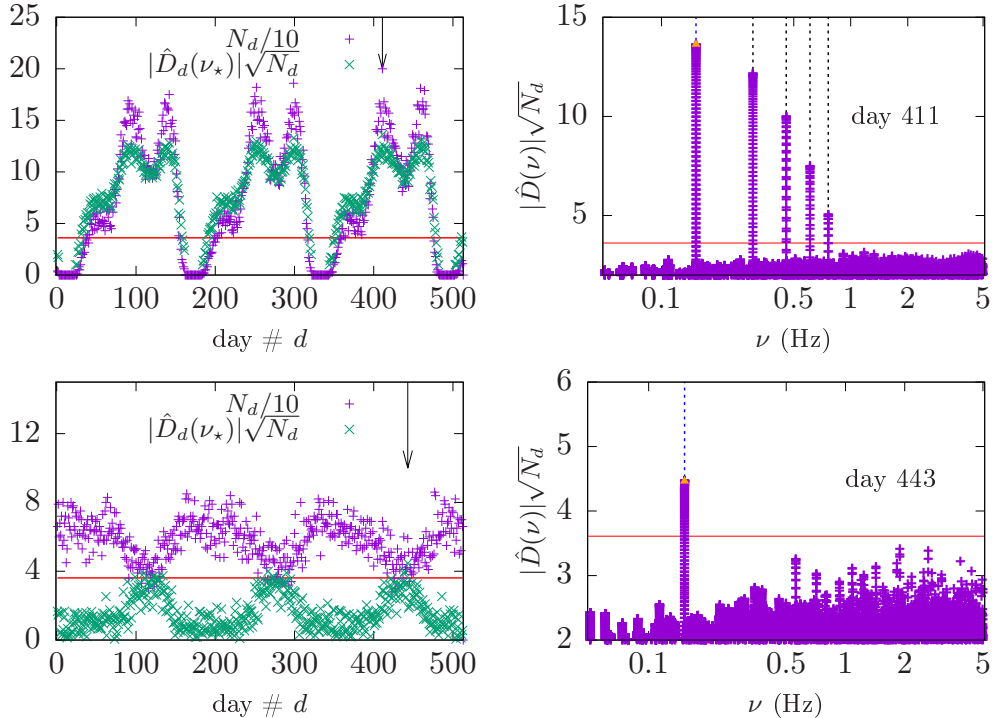


Figure 3. Results for the most promising days for spin frequency detection for two models with $P_p = 160$ d, $\Lambda = 0.2$ and $\epsilon_{\text{mag}} = 10^{-6}$. A pulsar-like model is shown in the top row and a hemisphere model in the bottom row. See Table 3 for details. Left panels show the number of bursts per day, N_d , divided by 10 (purple crosses) and the value of $|\hat{D}_d(\nu_*)|/\sqrt{N_d}$ on each day (green x's). Downward pointing arrows indicate the day with largest value of $|\hat{D}_d(\nu_*)|/\sqrt{N_d}$, days 411 (top/pulsar-like) and 443 (bottom/hemisphere) respectively. Right panels show results of computing $|\hat{D}_d(\nu)|/\sqrt{N_d}$ on these days for frequencies $0.05 \text{ Hz} \leq \nu \leq 5 \text{ Hz}$ with equal logarithmic spacing $\Delta\nu/\nu \simeq 10^{-5}$. Horizontal red lines are at $|\hat{D}_d(\nu)|/\sqrt{N_d} = \sqrt{\ln N_{\text{freq}}} \simeq 3.611$, the value above which about one point ought to appear at random according to the Rayleigh distribution. For the models shown, detecting the spin frequency ought to be relatively easy: the fundamental and four harmonics show up significantly for pulsar like model but just the fundamental for hemisphere model.

4. CONCLUSIONS

The first part of this paper has been devoted to the theory of precession of neutrons stars whose distortions are due to strong internal magnetic fields. We have stressed that unless internal field strengths are very large precession ought to be frustrated by pinning of neutron superfluid vortices, to nuclei in the crust (Shaham 1977) and to flux tubes associated with Type II proton superconductivity in the core (Link 2003). We argue that internal magnetic fields with strength $\gtrsim 10^{16}$ Gauss must pervade the star if precession is to be possible. As we have discussed, fields this strong can prevent proton superconductivity in the core (see Eq. (1) and associated discussion), are strong enough to shatter the crust and may even prevent or at least substantially alter neutron superfluidity in both core and crust (see Eq. (3) and associated discussion). Avoiding vortex line pinning is a very stringent requirement: even very localized regions where neutron vortices pin can prevent slow precession if they comprise just a modest fraction – say 0.1% – of the moment of inertia of the star (Shaham 1977).

These considerations led us to examine implications of a three component model of the magnetic field in magnetars: (1) a dipole component with characteristic strength $\sim 10^{14}$ Gauss; (2) a toroidal component with characteristic strength $\sim 10^{15} - 10^{16}$ Gauss; and (3) a disordered field with characteristic strength $\sim 10^{16}$ Gauss. Because the volume occupied by the toroidal field may be limited (as in the models of Akgün et al. (2013)) the disordered component may be critical for suppressing superfluidity and superconductivity, which is a necessary condition for slow precession. Since small-scale, disordered fields may decay in a timescale ~ 1000 years (see Eq. (28) and Reisenegger & Goldreich (1992), Glampedakis et al. (2011), Passamonti et al. (2017) and Gusakov et al. (2017)) a magnetar may only precess for a relatively short time, until the disordered field that enables slow precession decays significantly. The decay of the disordered field may also end the bursting phase in the life of a magnetar, for this component contains most of the

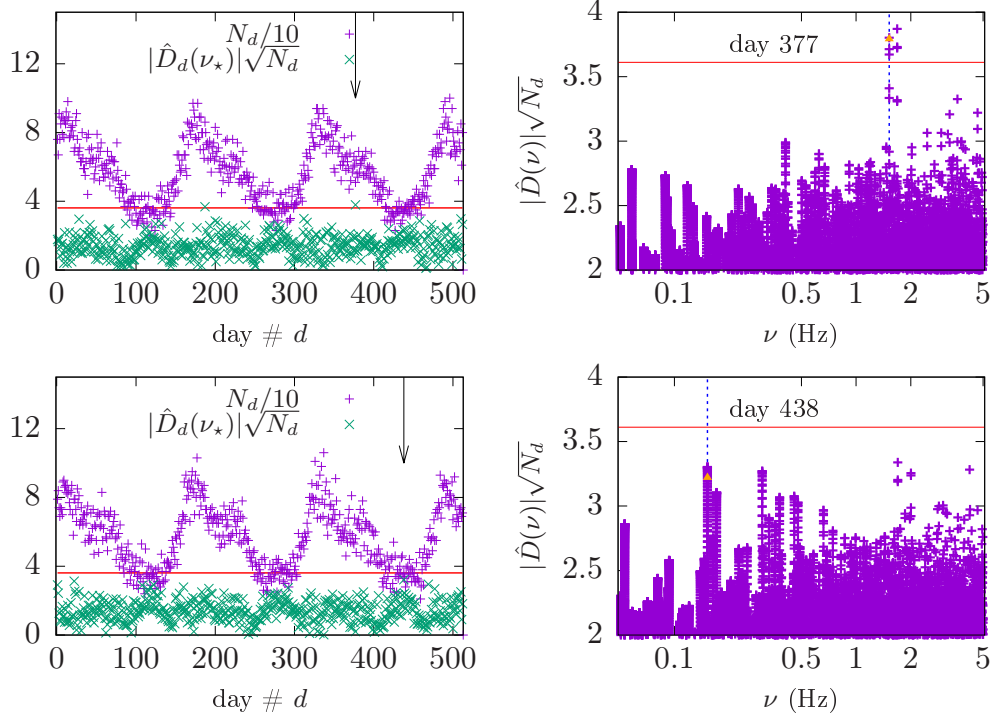


Figure 4. Results for the most promising days for spin frequency detection for two inter-cone models with $P_p = 160$ d, $\Lambda = 0.2$ and $\epsilon_{\text{mag}} = 10^{-7}$ (top) and $\epsilon_{\text{mag}} = 10^{-6}$ (bottom). The format is the same as in Fig. 3. For these models the spin frequency is not detectable unambiguously on their respective most promising days.

stellar magnetic energy and is capable of stimulating internal fluctuations that propagate into the magnetosphere, where they might trigger burst activity.

Illustrative but schematic models for magnetic distortion in §2.2 imply that the resulting quadrupolar deformation is almost certainly triaxial and probably prolate. We developed the theory of triaxial precession in §2.3, noting in particular that large amplitude precession can be excited as a result of small shearing motions involving only tiny fractions of the magnetic energy of the star. We included spindown in the theory developed in this section (using the spindown formula found by Li et al. (2012)): §2.4 develops a timing model $t(\Phi)$ that relates clock time to precession phase when spindown is included, and §2.5 develops the secular effects of spindown on precession dynamics for the triaxial case, a generalization of Goldreich (1970) which dealt with axisymmetric, oblate precession. We have yet to explore possible phenomenological implications of the secular evolution. The timing model exhibits the expected systematic spindown, as altered by precession, but also includes important cyclical terms that vary periodically with precession (discussed less generally by Cordes (1993)).

In the introduction, we asked whether the spin frequency ought to be detected for a magnetar precessing with a known precession period. So far, no spin frequency is apparent in either FRB 121102 or FRB 180916.J0158+65. This may be simply because we have not detected enough bursts from these FRBs to find evidence for their spin periods, or it may be that doing so is virtually impossible because of physical properties of these objects and the FRB mechanism. If the reason we have yet to detect spin frequencies is that we need more burst detections, how sensitive and systematic must an observing program be to find the spin convincingly?

In order to address this issue we constructed a specific stochastic model for FRBs in §3. In this model, FRBs are associated with outbursts that occur randomly in time with energy output that is beamed into a range of directions that we select. Generally, we confine the beam directions to be outward relative to a reference (magnetic) axis; for beam directions that are totally random neither the spin frequency nor the precession period is discernible. Thus, the existence of repeated precession cycles for FRB 121102 and FRB 180916.J0158+65 already shows that they are not caused by beamed emission directed entirely at random.

Our model offers some hope for detecting spin frequencies, as precession implies that there is a bias that favors detection of optimally directed beams. The analytic model in Appendix B demonstrates that the dependence on both

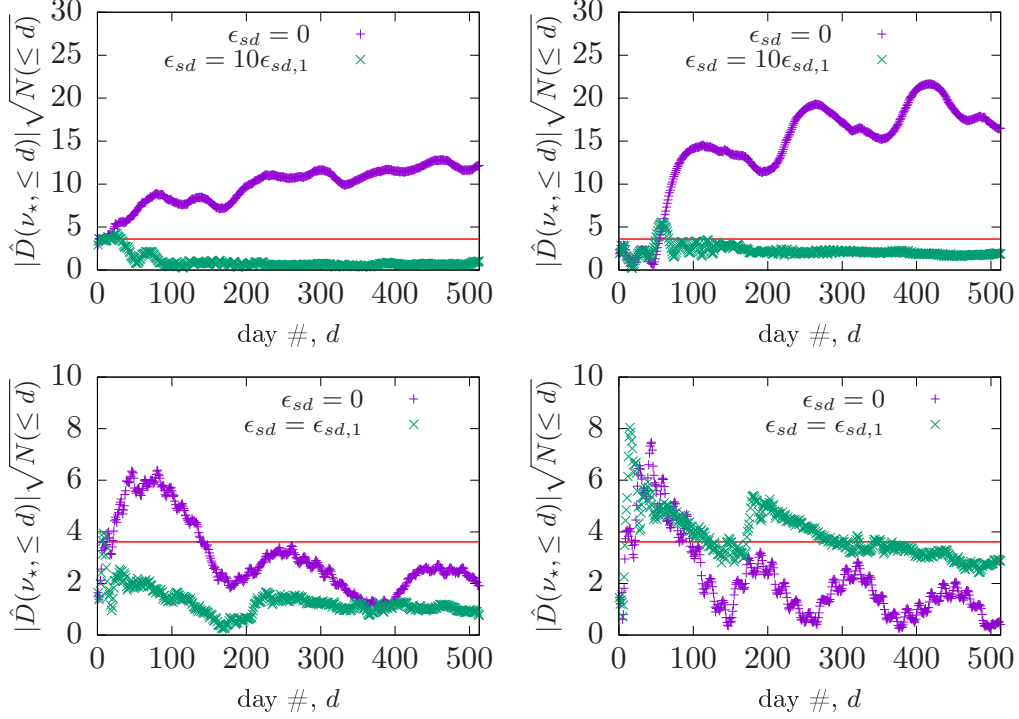


Figure 5. Cumulative $|\hat{D}(\nu_*, \leq d)|\sqrt{N(\leq d)}$ as a function of day number d . Top: $P_p = 160$ d, $\epsilon_{\text{mag}} = 10^{-6}$ nested-cone models with $\Lambda = 0.2$ (left) and $\Lambda = 0.44$ (right), and $\epsilon_{sd} = 0$ (purple crosses) and $\epsilon_{sd} = 10\epsilon_{sd,1}$ (green x's). Bottom: $P_p = 16.4$ d, $\epsilon_{\text{mag}} = 10^{-5}$ with $\Lambda = 0.2$ (left) and $\Lambda = 0.44$ (right), and $\epsilon_{sd} = 0$ (purple crosses) and $\epsilon_{sd} = \epsilon_{sd,1}$ (green x's).

the spin and precession frequencies arise from the motion of the unit vector to the observer in the rotating frame of reference, but the dependencies may be very weak. In order to assess whether or not the spin frequency can be detected, we computed $r_d(\nu_*) = |\hat{D}_d(\nu_*)|\sqrt{N_d}$ for each day d in our hypothetical observing program; N_d is the number of bursts detected on day d and $\hat{D}(\nu)$ is defined in Eq. (71). For a frequency search with $N_{\text{freq}} = 460518$ frequencies spanning the range $0.05 - 5$ Hz with equal logarithmic spacing, $\Delta\nu/\nu = 10^{-5}$, on any given day, the largest value that should arise at random is approximately $r_1(N_{\text{freq}}) = \sqrt{\ln N_{\text{freq}}} \approx 3.611$. The spin frequency ought to be detectable on days when $r_d(\nu_*) > r_1(N_{\text{freq}})$. Finding ν_* is likelier for cases where the number of days with $r_d(\nu_*) > r_1(N_{\text{freq}})$ is a substantial fraction of the total number of days on which observations are done.

Although we have only computed a modest number of models, the results reported in Table 3 divide qualitatively into two classes depending on the value of $q^2 = e^2\Lambda^2/(1 - \Lambda^2)$. Based on the criterion described above, we believe that detecting the burst frequency is likely when $q^2 > 1$ irrespective of the value of ϵ_{mag} or the distribution of beam directions. However, the situation for $q^2 < 1$ is more complicated. Although detecting ν_* ought to be easy for pulsar-like models, where the range of beam directions relative to the reference axis is small, widening this range diminishes the odds of detection considerably. Allowing beam directions anywhere in the outward hemisphere relative to the axis would lead to detections on $\lesssim 3\%$ of the days during which observations are done. But, restricting beams to avoid directions moderately close to the axis and perpendicular to it makes detecting the spin frequency is nearly impossible in our models.

Finally, the simulations all indicate that the fraction of outbursts that are ultimately detectable is small: the largest fraction of all outbursts that were detectable in our models was 3.9%, for pulsar-like models with $q^2 < 1$, and is at most 2.9% for all other models we have simulated. That means that the model simulated here is not very energy-efficient, in that at least $\sim 25 - 50$ times as much energy is being emitted in FRBs than we would deduce from observations. One might expect that beaming mitigates the energetic requirements, and of course for a given peak intensity the total emitted intensity is $\propto 1/\kappa \sim \theta_{\text{FWHM}}^2$. Our calculations only cover a single Gaussian beam width, $\theta_{\text{FWHM}} = 20^\circ$. Lowering θ_{FWHM} reduces the total number of detections at fixed outburst rate, which we have found to be roughly $\propto \theta_{\text{FWHM}}^2$ via sporadic exploration of the phase space. Assuming this to be true, the overall amount of energy required in the stochastic model would be roughly independent of θ_{FWHM} for small values of the beam width: the total emission

per beam is $\propto \theta_{\text{FWHM}}^2$ but the number of undetected beams per detected beam is $\propto 1/\theta_{\text{FWHM}}^2$. Moreover, with fewer burst detections per day uncovering the magnetar spin frequency becomes harder.

APPENDIX

A. USEFUL INTEGRALS AND DETAILS OF COMPUTING THE TIMING MODEL

Table 4. Useful Integrals and Averages

Integral ^a	Result
$\int_0^\Phi d\Phi' \text{dn}(\Phi')$	$\varphi(\Phi)$
$\int_0^\Phi d\Phi' \text{cn}\Phi' \text{dn}\Phi'$	$\text{sn}\Phi$
$\int_0^\Phi d\Phi' \text{sn}\Phi' \text{dn}\Phi'$	$-\text{cn}\Phi$
$\int_0^\Phi d\Phi' \text{cn}\Phi' = \int_0^{\varphi(\Phi)} \frac{d\varphi \cos \varphi}{\sqrt{1-Q^2 \sin^2 \varphi}}$	$\frac{\sin^{-1}[Q \sin \varphi(\Phi)]}{Q}$ ^b
$\int_0^\Phi d\Phi' \text{sn}\Phi' = \int_0^{\varphi(\Phi)} \frac{d\varphi \sin \varphi}{\sqrt{1-Q^2+Q^2 \cos^2 \varphi}}$	$\frac{1}{Q} \ln \left[\frac{1+Q}{Q \text{cn}\Phi + \sqrt{Q^2 \text{cn}^2\Phi + 1 - Q^2}} \right] = \frac{1}{Q} \ln \left[\frac{\text{dn}(\Phi) - Q \text{cn}(\Phi)}{1-Q} \right]$
$\int_0^\Phi d\Phi' \text{sn}^2\Phi'$	$\frac{1}{Q^2} [F(\varphi(\Phi) Q) - E(\varphi(\Phi) Q)]$
$\int_0^\Phi d\Phi' \text{sn}\Phi' \text{cn}\Phi'$	$E(\varphi Q) = \int_0^\varphi d\varphi' \sqrt{1-Q^2 \sin^2 \varphi'}$
$\langle \text{sn}^2\Phi \rangle$	$-\frac{\text{dn}\Phi}{Q^2}$
$\langle \text{dn}\Phi \rangle$	$\frac{1}{Q^2} \left[1 - \frac{E(\pi/2 Q)}{F(\pi/2 Q)} \right]$
$\langle \frac{1}{\text{dn}\Phi} \rangle$	$\frac{\pi/2}{F(\pi/2 Q)}$
$\langle \frac{\text{sn}^2\Phi}{\text{dn}\Phi} \rangle$	$\frac{\pi/2}{F(\pi/2 Q)\sqrt{1-Q^2}}$
$\langle \frac{\text{cn}^2\Phi}{\text{dn}\Phi} \rangle$	$\frac{\pi/2}{Q^2 F(\pi/2 Q)} \left(\frac{1}{\sqrt{1-Q^2}} - 1 \right)$
	$\frac{\pi/2}{Q^2 F(\pi/2 Q)} \left(1 - \sqrt{1-Q^2} \right)$

^a $Q = q$ for $q < 1$ and $Q = 1/q$ for $q > 1$.

^b $-\pi/2 \leq \sin^{-1}z \leq \pi/2$.

Using Table 4 we find

$$\begin{aligned}
\int_0^\Phi d\Phi' \int_0^{\Phi'} d\Phi'' \text{cn}\Phi'' \text{sn}\Phi'' &= \frac{1}{Q^2} \int_0^\Phi d\Phi' (1 - \text{dn}\Phi') = \frac{\Phi - \varphi(\Phi)}{Q^2} = \frac{\Phi(1 - \langle \text{dn}\phi \rangle)}{Q^2} + \frac{\Phi \langle \text{dn}\Phi \rangle - \varphi(\Phi)}{Q^2} \\
&\equiv \frac{\Phi(1 - \langle \text{dn}\phi \rangle)}{Q^2} + C_2(\Phi|Q) \\
\int_0^\Phi d\Phi' \int_0^{\Phi'} d\Phi'' \text{cn}\Phi'' \text{dn}\Phi'' &= \int_0^\Phi d\Phi' \text{sn}\Phi' = \frac{1}{Q} \ln \left[\frac{\text{dn}(\Phi) - Q \text{cn}(\Phi)}{1-Q} \right] \equiv C_3(\Phi|Q) \\
\int_0^\Phi d\Phi' \int_0^{\Phi'} d\Phi'' \text{sn}\Phi'' \text{dn}\Phi'' &= \int_0^\Phi d\Phi' (1 - \text{cn}\Phi') = \Phi - \frac{\sin^{-1}[Q \sin \varphi(\Phi)]}{Q} \equiv \Phi - C_4(\Phi|Q) \tag{A1}
\end{aligned}$$

where we rewrote the first integral to isolate the secular term from the strictly periodic one. The third integral also has a secular term. These terms are $\propto \Phi \propto \phi$ and, in effect, renormalize the initial spin period.

Finally, we consider terms $\propto \text{sn}^2\Phi$; we clearly need to remove $\langle \text{sn}^2\Phi \rangle$, which produces a term in $t(\phi)$ that is $\propto \phi^2$. We assume that what remains is periodic, so we focus just on the period starting at $\Phi = 0$. We then find

$$\begin{aligned}
C_1(\Phi|Q) &\equiv \int_0^\Phi d\Phi' \int_0^{\Phi'} d\Phi'' (\text{sn}^2\Phi'' - \langle \text{sn}^2\Phi \rangle) = \int_0^\Phi \frac{d\Phi' [F(\varphi(\Phi'))|Q] - E(\varphi(\Phi')|Q)]}{Q^2} - \frac{\langle \text{sn}^2\Phi \rangle \Phi^2}{2} \\
&= \frac{\Phi^2}{2} \left(\frac{1}{Q^2} - \langle \text{sn}^2\Phi \rangle \right) - \frac{1}{Q^2} \int_0^\Phi d\phi' E(\varphi(\Phi')) = \frac{\Phi^2 E(\pi/2|Q)}{2Q^2 F(\pi/2|Q)} - \frac{1}{Q^2} \int_0^\Phi d\Phi' E(\varphi(\Phi')|Q). \tag{A2}
\end{aligned}$$

Available routines for evaluating complete elliptic functions return values for $\varphi(\Phi) \leq \pi/2$ (Press et al. 2002) which covers all of the values of these functions; for $\pi/2 < \varphi \leq \pi$ we substitute

$$E(\varphi|Q) = E(\pi|Q) - E(\pi - \varphi|Q) = 2E(\pi/2|Q) - E(\pi - \varphi|Q) \quad (\text{A3})$$

to get

$$\begin{aligned} \int_0^\Phi d\Phi' E(\Phi'|Q) &= \int_0^{\pi/2} \frac{d\varphi E(\varphi|Q)}{\sqrt{1 - q^2 \sin^2 \varphi}} + 2E(\pi/2|Q)(\Phi - F(\pi/2|Q)) - \int_{\pi/2}^{\varphi(\Phi)} \frac{d\varphi' E(\pi - \varphi'|Q)}{\sqrt{1 - Q^2 \sin^2 \varphi'}} \\ &= \int_0^{\pi/2} \frac{d\varphi E(\varphi|Q)}{\sqrt{1 - q^2 \sin^2 \varphi}} + 2E(\pi/2|Q)(\Phi - F(\pi/2|Q)) - \int_{\pi - \varphi(\Phi)}^{\pi/2} \frac{d\psi E(\psi|Q)}{\sqrt{1 - Q^2 \sin^2 \psi}} \\ &= 2E(\pi/2|Q)(\Phi - F(\pi/2|Q)) + \int_0^{\pi - \varphi(\Phi)} \frac{d\psi E(\psi|Q)}{\sqrt{1 - Q^2 \sin^2 \psi}}. \end{aligned} \quad (\text{A4})$$

$C_1(\Phi|Q) = 0$ at $\Phi = 0$ and $\Phi = 2F(\pi/2|Q)$, and has its peak value at $\Phi = F(\pi/2|Q)$.

Fig. 6 shows results for $C_i(\Phi|Q)$ for one precession cycle for $Q = 0.3, 0.6$ and 0.9 , and also for $Q = 0$ (thin black line), for which the limiting forms are

$$C_1(\Phi) = \frac{\cos 2\Phi - 1}{8} \quad C_2(\Phi) = -\frac{\sin 2\Phi}{8} \quad C_3(\Phi) = 1 - \cos \Phi \quad C_4(\Phi) = \sin \Phi. \quad (\text{A5})$$

The functions $C_1(\Phi|q)$ and $C_2(\Phi|q)$ have periods equal to half of the precession period. The functions $C_3(\Phi|q)$ and $C_4(\Phi|q)$ have periods equal to a full precession cycle. Notice that although there is no secular variation of $C_3(\Phi|q)$ this function has a nonzero mean over its full cycle of variation, which would manifest itself as a offset in $t(\phi)$.

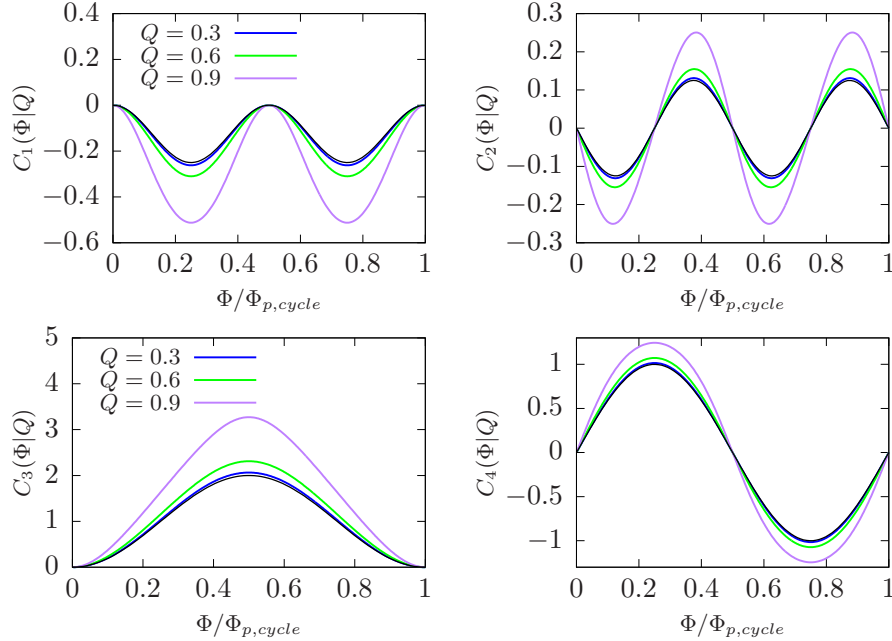


Figure 6. $C_i(\Phi|Q)$ versus Φ for one precession cycle and $Q = 0, 0.3, 0.6$ and 0.9 .

B. ANALYTIC THEORY OF DETECTION PROBABILITY

Eq. (68) relates the intrinsic intensity I and the peak intensity $I(1)$; in our model a burst is detectable if $I > I_{\min}$. The probability that a burst with peak intensity $I(1)$ is detectable at precession phase Φ is

$$P_{\text{detect}}(I(1), \Phi) = \int d^2 \hat{\mathbf{b}} n(\hat{\mathbf{b}}) \Theta(I - I_{\min}) = \int d^2 \hat{\mathbf{b}} n(\hat{\mathbf{b}}) \Theta \left(I(1) \exp[\kappa(\hat{\mathbf{b}} \cdot \hat{\mathbf{n}}(\Phi) - 1)] - I_{\min} \right),$$

where $n(\hat{\mathbf{b}})$ is the distribution of beam directions (normalized to one) and $\Theta(\dots)$ is the Heaviside function; use

$$\begin{aligned}\Theta\left(I(1)\exp[\kappa(\hat{\mathbf{b}}\cdot\hat{\mathbf{n}}(\Phi)-1)]-I_{\min}\right) &= \Theta\left(\frac{I(1)}{I_{\min}}\exp[\kappa(\hat{\mathbf{b}}\cdot\hat{\mathbf{n}}(\Phi)-1)]-1\right) \\ &= \Theta(\ln(I(1)/I_{\min})+\kappa[\hat{\mathbf{b}}\cdot\hat{\mathbf{n}}(\Phi)-1]) = \Theta(\kappa^{-1}\ln(I(1)/I_{\min})-1+\hat{\mathbf{b}}\cdot\hat{\mathbf{n}}(\Phi))\end{aligned}$$

to rewrite as

$$P_{\text{detect}} = \int d^2\hat{\mathbf{b}} n(\hat{\mathbf{b}}) \Theta(\kappa^{-1}\ln(I(1)/I_{\min})-1+\hat{\mathbf{b}}\cdot\hat{\mathbf{n}}(\Phi)).$$

In a right handed coordinate system defined by unit vectors $\hat{\mathbf{e}}_a, \hat{\mathbf{e}}_b, \hat{\boldsymbol{\mu}}$ let

$$\hat{\mathbf{n}}(\Phi) = \hat{\boldsymbol{\mu}} \cos \theta_n + \sin \theta_n (\hat{\mathbf{e}}_a \cos \varphi_n + \hat{\mathbf{e}}_b \sin \varphi_n),$$

so that

$$\hat{\mathbf{b}}\cdot\hat{\mathbf{n}}(\Phi) = \cos \theta_b \cos \theta_n + \sin \theta_b \sin \theta_n \cos(\varphi_b - \varphi_n) \equiv \cos \theta_b \cos \theta_n + \sin \theta_b \sin \theta_n \cos \tilde{\varphi}_b;$$

then the Heaviside function requires that

$$1 \geq \cos \theta_b \cos \theta_n + \sin \theta_b \sin \theta_n \cos \tilde{\varphi}_b > 1 - \frac{\ln(I(1)/I_{\min})}{\kappa},$$

and therefore $\hat{\mathbf{b}}\cdot\hat{\mathbf{n}}(\Phi)$ must be close to one for very large values of κ . Thus if we define $\theta_b = \theta_n + \delta_b$ where $\delta_b \ll 1$ and assume that $\tilde{\varphi}_b \ll 1$

$$\cos \theta_b \cos \theta_n + \sin \theta_b \sin \theta_n \cos \tilde{\varphi}_b = \cos(\theta_b - \theta_n) + \sin \theta_b \sin \theta_n (\cos \tilde{\varphi}_b - 1) \approx 1 - \frac{1}{2} (\delta_b^2 + \sin^2 \theta_n \tilde{\varphi}_b^2)$$

and the Heaviside function requires that

$$1 \geq 1 - \frac{1}{2} (\delta_b^2 + \sin^2 \theta_n \tilde{\varphi}_b^2) > 1 - \frac{\ln(I(1)/I_{\min})}{\kappa} \Rightarrow 0 \leq \delta_b^2 + \sin^2 \theta_n \tilde{\varphi}_b^2 < \frac{2\ln(I(1)/I_{\min})}{\kappa} \equiv R^2.$$

We assume that $n(\hat{\mathbf{b}}) = \tilde{n}(\cos \theta_b)/2\pi$ is only a function of $\cos \theta_b$; with this assumption

$$d^2\hat{\mathbf{b}} n(\hat{\mathbf{b}}) = \frac{d\varphi}{2\pi} d\cos \theta_b \tilde{n}(\cos \theta_b) \simeq \frac{d\tilde{\varphi}_b}{2\pi} d\delta_b \sin \theta_n \tilde{n}(\cos \theta_n)$$

With these substitutions we find

$$\begin{aligned}P_{\text{detect}}(I(1), \Phi) &\simeq \int_{-R}^{+R} d\delta_b \sin \theta_n \tilde{n}(\cos \theta_n) \int_{-\sqrt{R^2-\delta_b^2}/\sin \theta_n}^{+\sqrt{R^2-\delta_b^2}/\sin \theta_n} \frac{d\tilde{\varphi}_b}{2\pi} \\ &= \frac{2R^2\tilde{n}(\cos \theta_n)}{\pi} \int_0^1 dx \sqrt{1-x^2} = \frac{\tilde{n}(\cos \theta_n) \ln(I(1)/I_{\min})}{\kappa}.\end{aligned}\quad (\text{B1})$$

1. P_{detect} increases with increasing $I(1)$ weakly, decreases $\propto 1/\kappa$ as κ increases, and is only nonzero where $n(\cos \theta_n) \neq 0$.
2. If $\tilde{n}(\cos \theta_b)$ is uniform, as would be the case if beam directions are random and isotropic, then there is no Φ dependence so there is no imprint of either the spin frequency or precession frequency on P_{detect} .
3. Φ dependence arises from nonuniformity in $\tilde{n}(\cos \theta_b)$; in our models, nonuniformity is a consequence of boundaries in the distribution of beam directions.

Consider the region near θ_{\max} . If $\theta_{\max} - R < \theta_n < \theta_{\max}$ and $\tilde{n}(\cos \theta_b) = 0$ at $\theta_b > \theta_{\max}$ then

$$P_{\text{detect}}(I(1), \Phi) \simeq \frac{\tilde{n}R}{\pi} \int_{-R}^{\theta_{\max}-\theta_n} d\delta_b \sqrt{1-\delta_b^2/R^2} = \frac{\tilde{n}R^2}{\pi} \left[\frac{\pi}{4} + \frac{1}{2} \left(\sin^{-1} \Delta + \Delta \sqrt{1-\Delta^2} \right) \right] \quad (\text{B2})$$

where $\Delta = (\theta_{\max} - \theta_n)/R < 1$ and \tilde{n} is the uniform value inside the region containing beams; if $\theta_n > \theta_{\max}$ then $-R < \delta_b < \theta_{\max} - \theta_n < 0$ and

$$P_{\text{detect}}(I(1), \Phi) = \frac{\tilde{n}R}{\pi} \int_{-R}^{\theta_{\max}-\theta_n} d\delta_b \sqrt{1-\delta_b^2/R^2} = \frac{\tilde{n}R^2}{\pi} \left[\frac{\pi}{4} - \frac{1}{2} \left(\sin^{-1} |\Delta| + |\Delta| \sqrt{1-\Delta^2} \right) \right]. \quad (\text{B3})$$

Eq. (B2) can be used for θ_n inside or outside provided that we use $\sin \Delta = -\sin |\Delta|$ for $\Delta < 0$. Near θ_{\min} , similar considerations imply that $-1 < \delta_b < \theta_n - \theta_{\min}$; then we get the same results but with $\Delta = (\theta_n - \theta_{\min})/R$. For $\theta_{\min} = 0$, $0 \leq \delta_b \leq \theta_n$ ($0 \leq \Delta \leq 1$). Otherwise, $P_{\text{detect}} = 0$ for $\theta_n \leq \theta_{\min} - R$ and for $\theta_n > \theta_{\max} + R$. These results depend on Φ via Δ and imprint information about both the spin frequency and the precession cycle on our models. We also note that the range of values θ_n is model dependent via Λ , e^2 , and the rate at which outbursts occur, which may depend on Φ (but doesn't in our models). If $R(\Phi, I(1))dI(1)d\Phi$ is the rate of outbursts with intrinsic intensity in $I(1) + dI(1)$ then

$$dr_{\text{detect}}(\Phi) = d\Phi \int dI(1)R(I(1), \Phi)P_{\text{detect}}(I(1), \Phi) \quad (\text{B4})$$

is the rate of detection of bursts in $d\Phi$.

These results can be generalized to beams distributed about multiple axes by replacing

$$n(\hat{\mathbf{b}}) \rightarrow \sum_j p_j n_j(\hat{\mathbf{b}})$$

where p_j is the probability that a beam comes from the distribution around the axis $\hat{\boldsymbol{\mu}}_j$ and $n_j(\hat{\mathbf{b}})$ is normalized to one. The average beam direction is then the sum of $p_j \langle \hat{\mathbf{b}}_j \rangle$.

- 1 SC and JMC acknowledge support from the National Science Foundation (NSF) under AAG award 1815242 and are
- 2 members of the NANOGrav Physics Frontiers Center supported by NSF award 1430284. IW thanks Jeevak Parpia,
- 3 Armen Sedrakian and Peter Rau for helpful comments.

REFERENCES

- Abramowitz, M., & Stegun, I. A. 1972, Handbook of Mathematical Functions
- Akgün, T., Link, B., & Wasserman, I. 2006, MNRAS, 365, 653, astro-ph/0506606
- Akgün, T., Reisenegger, A., Mastrano, A., & Marchant, P. 2013, MNRAS, 433, 2445, 1302.0273
- Akgün, T., & Wasserman, I. 2008, MNRAS, 383, 1551, 0705.2195
- Alpar, M. A., Pines, D., Anderson, P. W., & Shaham, J. 1984, ApJ, 276, 325
- Anderson, P. W., Alpar, M. A., Pines, D., & Shaham, J. 1982, Philosophical Magazine, Part A, 45, 227
- Anderson, P. W., & Itoh, N. 1975, Nature, 256, 25
- Baym, G., Pethick, C., & Pines, D. 1969, Nature, 224, 673
- Braithwaite, J. 2009, MNRAS, 397, 763, 0810.1049
- Caplan, M. E., Schneider, A. S., & Horowitz, C. J. 2018, PhRvL, 121, 132701, 1807.02557
- Cardall, C. Y., Prakash, M., & Lattimer, J. M. 2001, ApJ, 554, 322, astro-ph/0011148
- Carreau, T., Gulminelli, F., Chamel, N., Fantina, A. F., & Pearson, J. M. 2020, A&A, 635, A84, 1912.01265
- Chandrasekhar, B. S. 1962, Applied Physics Letters, 1, 7
- Chime/Frb Collaboration et al. 2020, Nature, 582, 351, 2001.10275
- Clogston, A. M. 1962, PhRvL, 9, 266
- Cordes, J. M. 1993, in Astronomical Society of the Pacific Conference Series, Vol. 36, Planets Around Pulsars, ed. J. A. Phillips, S. E. Thorsett, & S. R. Kulkarni (Astronomical Society of the Pacific), 43–60
- Cruces, M. et al. 2021, MNRAS, 500, 448, 2008.03461
- Cutler, C. 2002, PhRvD, 66, 084025, gr-qc/0206051
- Dong, J. M., Lombardo, U., Zhang, H. F., & Zuo, W. 2017, Physics of Atomic Nuclei, 80, 77
- Friebe, J., & Rezzolla, L. 2012, MNRAS, 427, 3406, 1207.4035
- Fulde, P., & Ferrell, R. A. 1964, Physical Review, 135, 550
- Gezerlis, A., Pethick, C. J., & Schwenk, A. 2014, ArXiv e-prints, 1406.6109
- Glampedakis, K., Jones, D. I., & Samuelsson, L. 2011, MNRAS, 413, 2021, 1010.1153
- Glampedakis, K., & Lasky, P. D. 2016, MNRAS, 463, 2542, 1607.05576
- Goldreich, P. 1970, ApJL, 160, L11
- Goldreich, P., & Sridhar, S. 1995, ApJ, 438, 763
- Gottfried, K. 1966, Quantum mechanics - Vol.1: Fundamentals (Reading:W. A. Benjamin)
- Gourgouliatos, K. N., & Cumming, A. 2014a, PhRvL, 112, 171101, 1311.7345
- . 2014b, MNRAS, 438, 1618, 1311.7004
- Gourgouliatos, K. N., & Pons, J. A. 2020, arXiv e-prints, arXiv:2001.03335, 2001.03335

- Guo, W., Dong, J. M., Shang, X., Zhang, H. F., Zuo, W., Colonna, M., & Lombardo, U. 2019, *NuPhA*, 986, 18, 1810.02709
- Gusakov, M. E., Kantor, E. M., & Ofengeim, D. D. 2017, *PhRvD*, 96, 103012, 1705.00508
- Hashimoto, M., Seki, H., & Yamada, M. 1984, *Progress of Theoretical Physics*, 71, 320
- Haskell, B., & Sedrakian, A. 2018, in *Astrophysics and Space Science Library*, ed. L. Rezzolla, P. Pizzochero, D. I. Jones, N. Rea, & I. Vidaña, Vol. 457, 401
- Henriksson, K. T., & Wasserman, I. 2013, *MNRAS*, 431, 2986, 1212.5842
- Iroshnikov, P. S. 1963, *AZh*, 40, 742
- Jones, P. B. 1975, *Ap&SS*, 33, 215
- Kinnunen, J. J., Baarsma, J. E., Martikainen, J.-P., & Törmä, P. 2018, *Reports on Progress in Physics*, 81, 046401, 1706.07076
- Kiuchi, K., & Yoshida, S. 2008, *PhRvD*, 78, 044045, 0802.2983
- Kraichnan, R. H. 1965, *Physics of Fluids*, 8, 1385
- Lander, S. K., & Gourgouliatos, K. N. 2019, *MNRAS*, 486, 4130, 1902.02121
- Lander, S. K., & Jones, D. I. 2012, *MNRAS*, 424, 482, 1202.2339
- . 2017, *MNRAS*, 467, 4343, 1610.08745
- Larkin, A. I., & Ovchinnikov, Y. N. 1974, *Soviet Journal of Experimental and Theoretical Physics*, 38, 854
- Lasky, P. D., & Melatos, A. 2013, *PhRvD*, 88, 103005, 1310.7633
- Lee, T.-G., Yoshiike, R., & Tatsumi, T. 2018, in *Quarks and Compact Stars 2017 (QCS2017)*, 011006
- Levin, Y., Beloborodov, A. M., & Bransgrove, A. 2020, *ApJL*, 895, L30, 2002.04595
- Li, D. et al. 2021, *arXiv e-prints*, arXiv:2107.08205, 2107.08205
- Li, J., Spitkovsky, A., & Tchekhovskoy, A. 2012, *ApJ*, 746, 60, 1107.0979
- Li, X., Levin, Y., & Beloborodov, A. M. 2016, *ApJ*, 833, 189, 1606.04895
- Link, B. 2003, *Physical Review Letters*, 91, 101101, arXiv:astro-ph/0302441
- Link, B., & Cutler, C. 2002, *Monthly Notices of the Royal Astronomical Society*, 336, 211, <https://academic.oup.com/mnras/article-pdf/336/1/211/18417731/336-1-211.pdf>
- Link, B., Epstein, R. I., & Baym, G. 1993, *ApJ*, 403, 285
- Lorenz, C. P., Ravenhall, D. G., & Pethick, C. J. 1993, *PhRvL*, 70, 379
- Mestel, L., Nittmann, J., Wood, W. P., & Wright, G. A. E. 1981, *MNRAS*, 195, 979
- Mestel, L., & Takhar, H. S. 1972, *MNRAS*, 156, 419
- Mitchell, J. P., Braithwaite, J., Reisenegger, A., Spruit, H., Valdivia, J. A., & Langer, N. 2015, *MNRAS*, 447, 1213, 1411.7252
- Mutafchieva, Y. D., Chamel, N., Stoyanov, Z. K., Pearson, J. M., & Mihailov, L. M. 2019, *PhRvC*, 99, 055805, 1904.05045
- Nittmann, J., & Wood, W. P. 1981, *MNRAS*, 196, 491
- Passamonti, A., Akgün, T., Pons, J. A., & Miralles, J. A. 2017, *MNRAS*, 465, 3416, 1608.00001
- Pethick, C. J., & Potekhin, A. Y. 1998, *Physics Letters B*, 427, 7, astro-ph/9803154
- Potekhin, A. Y., & Chabrier, G. 2018, *A&A*, 609, A74, 1711.07662
- Press, W. H., Teukolsky, S. A., Vetterling, W. T., & Flannery, B. P. 2002, *Numerical recipes in C++ : the art of scientific computing*
- Rau, P. B., & Wasserman, I. 2021, *MNRAS*, 2104.08563
- Rau, P. B., & Wasserman, I. 2021, (in preparation)
- Ravenhall, D. G., Pethick, C. J., & Wilson, J. R. 1983, *PhRvL*, 50, 2066
- Reisenegger, A. 2009, *A&A*, 499, 557, 0809.0361
- Reisenegger, A., & Goldreich, P. 1992, *ApJ*, 395, 240
- Schneider, A. S., Caplan, M. E., Berry, D. K., & Horowitz, C. J. 2018, *PhRvC*, 98, 055801
- Shaham, J. 1977, *ApJ*, 214, 251
- Spitzer, Jr., L. 1958, in *IAU Symposium, Vol. 6, Electromagnetic Phenomena in Cosmical Physics*, ed. B. Lehnert, 169–+
- Suh, I.-S., & Mathews, G. J. 2010, *ApJ*, 717, 843, 1005.2139
- The CHIME/FRB Collaboration et al. 2021, *arXiv e-prints*, arXiv:2107.08463, 2107.08463
- Thompson, C., & Duncan, R. C. 1993, *ApJ*, 408, 194
- Wasserman, I. 2003, *MNRAS*, 341, 1020, arXiv:astro-ph/0208378
- Zanazzi, J. J., & Lai, D. 2020, *ApJL*, 892, L15, 2002.05752
- Zhang, Y. G., Gajjar, V., Foster, G., Siemion, A., Cordes, J., Law, C., & Wang, Y. 2018, *ApJ*, 866, 149, 1809.03043
- Zuo, W., Cui, C. X., Lombardo, U., & Schulze, H. 2008, *PhRvC*, 78, 015805